

This manuscript is titled '**Observations from the Seafloor: Ultra-low-frequency Ambient Ocean-Bottom Nodal Seismology at the Amendment Field**' with authors: **Aaron J. Girard** (aaron.j.girard@gmail.com), **Jeffrey Shragge** (jshragge@gmail.com), **Mike Danilouchkine** (mike.danilouchkine@shell.com), **Carsten Udengaard** (carsten.udengaard@tgs.com) and **Sijmen Gerritsen** (sijmen.gerritsen@shell.com). It has been submitted for review in **Geophysical Journal International**.

Please note that while this manuscript is undergoing peer-review, it has not been accepted for publication at the time of submission to EarthArxiv. Subsequent versions of the manuscript may have slightly different content. If accepted, the final version of this manuscript will be available via the 'Peer-reviewed Publication DOI' link on the EarthArxiv posting page. Please feel free to contact any authors with feedback.

1 **Observations from the Seafloor: Ultra-low-frequency Ambient** 2 **Ocean-Bottom Nodal Seismology at the Amendment Field**

3 A.J. Girard¹, J. Shragge¹, M. Danilouchkine², C. Udengaard³ and S. Gerritsen²

¹ *Center for Wave Phenomena, Department of Geophysics, Colorado School of Mines, Golden CO 80401, USA*

² *Shell Global Solutions International B.V., Carel van Bylandtlaan 16, 2596 HR, The Hague, The Netherlands*

³ *TGS, Houston TX 77041, USA*

4 Received 16 February 2024

5 **SUMMARY**

6 Large-scale ocean-bottom node (OBN) arrays of 1000s of multi-component instruments de-
7 ployed over 1000s of square kilometers have been used successfully for active-source seis-
8 mic exploration activities including full waveform inversion (FWI) at exploration frequencies
9 above about 2.0 Hz. The analysis of concurrently recorded lower-frequency ambient wavefield
10 data, though, is only just beginning. A key long-term objective of such ambient wavefield anal-
11 yses is to exploit the sensitivity of sub-2.0 Hz energy to build long-wavelength initial elastic
12 models, thus facilitating FWI applications. However, doing so requires a more detailed un-
13 derstanding of ambient wavefield information recorded on the seafloor, the types, frequency
14 structure and effective source distribution of recorded surface-wave modes, the near-seafloor
15 elastic model structure, and the sensitivity of recorded wave modes to subsurface model struc-
16 ture. To this end, we present a wavefield analysis of low- and ultra-low-frequency ambient
17 data (defined as <1.0 Hz and <0.1 Hz, respectively) acquired on 2712 OBN stations in the
18 Amendment Phase 1 survey covering 2750 km² of the Gulf of Mexico. After applying prestack
19 ambient data preprocessing and seismic cross-coherence interferometry workflows, we demon-
20 strate that the resulting virtual shot gather (VSG) volumes contain evidence for surface-wave
21 and guided P-wave mode propagation between the 0.01-1.0 Hz that remains coherent to dis-

22 tances of at least 80 km. Evidence for surface-wave scattering from near-surface salt-body
23 structure between 0.35-0.85 Hz is also present in a wide spatial distribution of VSG data. Fi-
24 nally, the interferometric VSG volumes clearly show waveform repetition at 20 s intervals in
25 sub-0.3 Hz surface-wave arrivals, a periodicity consistent with the mean active-source shot
26 interval. This suggests that the dominant contribution of surface-wave energy acquired in this
27 VSG frequency band is likely predominantly related to air-gun excitation rather than by natu-
28 rally occurring energy sources. Overall, these observations may have important consequences
29 for the early stages of initial model building for elastic FWI analysis.

30 **Key words:** Seismic array, Seismic noise, Exploration seismology, Rayleigh waves, Surface
31 waves

32 1 INTRODUCTION

33 Energy from compressed air guns recorded on towed streamer or ocean-bottom nodal (OBN) ar-
34 rays is commonly used for active-source seismic data acquisition for exploration activities. Typical
35 active-source processing strategies work to isolate energy of individual shots (or separated from
36 other contributions in simultaneous source acquisition), which are used in subsequent seismic
37 data processing, velocity model building, and migration imaging activities. While air-gun energy
38 sources long have been an industry staple and can provide energy rich in frequencies above roughly
39 2.0 Hz, they face significant technical limitations in generating sub-2.0 Hz energy at magnitudes
40 sufficient for high-end velocity model building. In particular, full waveform inversion (FWI) re-
41 quires starting earth models that are sufficiently accurate to enable the simulation of waveforms to
42 within a half wavelength of recorded data. Not satisfying this criterion causes cycle-skipping phe-
43 nomena that can lead to the FWI optimization processes not converging to the global minimum.
44 This has motivated much research in the development of expanding the lower-frequency band-
45 width of energy sources and the acquisition of longer source-receiver offset data, both of which
46 demonstrably improve the stability of FWI analyses (Pérez Solano & Plessix 2023).

47 A potential alternative source of low-frequency (i.e., sub-1.0 Hz) information is ambient seis-
48 mic wavefield energy. Naturally occurring energy, generated by swell-induced ocean gravity (and

49 potentially infragravity) waves with typical dominant periods between 1-25 s, is known to transfer
50 wavefield energy into the subsurface in the $10^{-3} - 10^0$ Hz frequency band (Longuet-Higgins 1950;
51 Webb 1998; Bromirski et al. 2005). This energy propagates predominantly as surface waves (i.e.,
52 Scholte, Love, and in some circumstances, leaky Rayleigh) at and below the seafloor at velocities
53 controlled by the elastic properties of the solid medium, the acoustic properties of sea water, and
54 with frequency-dependent wavefield magnitudes that generally decay away from the fluid-solid
55 interface. Ambient seismic waveforms have been observed throughout the world by, among oth-
56 ers, the longstanding Ocean Seismic Network of continuously recording seismometers typically
57 buried in shallow boreholes at 0.1 km depth below the seafloor (Stephen 1998). These high-quality
58 recordings with broadband sensitivity at frequencies between $10^{-3} - 10^3$ Hz have greatly improved
59 the seismology community's temporal understanding of microseism phenomena.

60 The growth in deployments of large-scale OBN arrays consisting of 1000s of recording stations
61 at fixed seafloor locations for up to three months presents an opportunity to greatly improve the
62 spatio-temporal understanding of marine ambient wavefield phenomena. OBN instruments gener-
63 ally consist of four-component (4-C) sensors with a triaxial geophone measuring one vertical and
64 two horizontal components embedded in the solid medium measuring vector particle velocity and
65 a single hydrophone sensor situated in the fluid layer measuring the scalar pressure field. OBN
66 geophones and hydrophone sensors usually have frequency corners between 2-15 Hz and thus (are
67 thought to) become decreasingly sensitive to ambient wavefield energy when progressing to de-
68 creasingly lower frequencies in the sub-1.0 Hz band. OBN recordings at frequencies lower than the
69 stated geophone and hydrophone corners also are subject to increasing magnitude and phase distor-
70 tions with decreasing frequency. This fact is commonly assumed to make high-fidelity individual
71 station observations challenging without applying careful instrumentation corrections. Thus, an
72 outstanding question is to what degree are ambient seismic wavefield data recorded on 4-C OBN
73 stations useful for low- and ultra-low-frequency seismic investigation (respectively defined herein
74 as < 1.0 Hz and < 0.1 Hz)?

75 Over the past decade, numerous researchers have investigated the OBN array response to low-
76 frequency maritime ambient seismic wavefield energy, usually in the context of seismic inter-

Reference	Name	Type	Area (km ²)	# of Stations	Inline Samp (m)	Xline Samp (m)
Bussat & Kugler (2011)	Astero	2-D OBN	126	140	1000	5 lines
de Ridder & Dellinger (2011)	Valhall	3-D OBC	45	2304	50	300
de Ridder & Biondi (2015)	Ekofisk	3-D OBC	66	3966	50	300
Girard et al. (2023)	Gulf of Mexico	3-D OBN	484	2014	369	426
Present study	Amendment	3-D OBN	2750	2712	1000	2000

Table 1. Notable references applying seismic ambient wavefield interferometry to data acquired on the ocean-bottom node (OBN) or cable (OBC) arrays.

ferometry. Olofsson (2010) investigates low-frequency ambient wavefield energy in the 1-10 Hz
frequency band recorded for a five-day period on the Astero OBN array located 70 km offshore
of the Norwegian coast. [Table 1 presents a list of notable ambient seismic wavefield interferom-
etry applied to ocean-bottom node (OBN) or cable (OBC) arrays.] Bussat & Kugler (2011) apply
ambient wavefield interferometry to the same North Sea data set and generate virtual shot gathers
(VSGs) that demonstrate the recovery of usable surface-wave waveforms to as low as 0.1 Hz. That
work subsequently uses the recovered VSG data to constrain the shear-wave velocity structure to
4.0 km depth. de Ridder & Dellinger (2011) demonstrates the use of ambient noise eikonal tomog-
raphy results for near-seabed imaging at the North Sea Valhall field. de Ridder & Biondi (2015)
presents a further case study of ambient seismic noise tomography at the North Sea Ekofisk field.
Girard et al. (2023) apply a prestack ambient processing workflow (Girard & Shragge 2020) to
data acquired in the 0.3-1.6 Hz frequency band on a Gulf of Mexico (GoM) OBN array. The en-
suing interferometric results clearly demonstrate the ability to recover surface-wave information
between 0.3-0.8 Hz as well as waveform sensitivity to large-scale salt structure.

While these studies successfully demonstrate that ambient wavefield data acquired on the
ocean bottom can be processed to generate coherent wave propagation across recording arrays and
that the resulting waveforms can be used in seismic imaging and inversion investigations, a number
of important questions remain about the limits of this style of ambient seismic OBN investigation:

95 (1) can coherent ambient waveforms be recovered by seismic interferometry on dense OBN ar-
96 rays significantly larger than the typically reported 100-400 km² area with sampling sparser than
97 the 4-16 stations per km²? (2) are conventional 4-C OBN instruments capable of recovering usable
98 coherent ambient wavefield information at low- and ultra-low frequencies? (3) does ambient wave-
99 field information extracted at these frequencies on conventional instruments coherently propagate
100 over distances ranging up to 80 km? and (4) what are the implications for long-wavelength elastic
101 model building [e.g., ambient FWI (Sager et al. 2018; de Ridder & Maddison 2018)]?

102 To examine these questions we use continuous low-frequency ambient wavefield recordings
103 from the Amendment Phase 1 OBN survey, which covers 2750 km² of the Mississippi Canyon
104 and Atwater Valley regions of the GoM. We note that while the large-scale active-source OBN
105 survey was not originally intended for ambient wavefield investigations, the deployment featured
106 a 35-day period when 2750 OBN stations were continuously and simultaneously recording. This
107 extended period of synchronous data acquisition greatly facilitates the extraction and analysis of
108 low-frequency energy, prestack ambient processing for data conditioning, and seismic interfer-
109 ometry for estimating VSGs with virtual source-receiver offsets reaching over 80 km in length.
110 Thus, a key objective of this work is presenting the results and observations of applying a prestack
111 ambient data processing workflow and seismic interferometry to this unique OBN data set.

112 The paper begins with an overview and characteristics of the Amendment Phase 1 OBN data set
113 and a description of the prestack ambient processing and cross-coherence seismic interferometry
114 workflows applied to estimate the VSGs. We then present results in terms of frequency decom-
115 posed VSGs and illustrate observed surface-wave propagation at the seafloor for the vertical and
116 pressure (Z and P) components including a repeating waveform with a 20 s period that we attribute
117 to air-gun contributions excited with the same periodicity. After investigating the observed wave
118 modes and spatial heterogeneity of observations as a function of absolute offset, we present obser-
119 vations of significant surface-wave scattering from subsurface structure. The paper concludes with
120 a discussion on the potential benefits and inversion opportunities provided by ultra-low-frequency
121 ambient wavefield observations on large-scale OBN arrays.

2 AMENDMENT OBN DATA SET

The Amendment Phase 1 OBN data set was acquired by TGS for an approximately 122-day period in 2019 (Roende et al. 2020). A total of 2750 4-C OBNs were deployed over a roughly 80 km by 40 km area in a staggered grid pattern with 1.0 km mean station spacing in both the inline and crossline directions. The survey covers water depths ranging from 0.60 km to 2.07 km. The deployed ZXPLR nodal hardware used a chip-scale atomic clock for timing accuracy and 3 Hz hydrophone and 15 Hz triaxial geophone as sensing elements. Sensor hardware settings included 0 dB and 6 dB preamp gains on the hydrophone and geophones, respectively.

Continuous OBN field records received at Colorado School of Mines from TGS were partitioned into 30-minute recordings, with separate files for each of the four components. Because this experiment focused on low-frequency data, continuous waveform data were low-passed with a 4.0 Hz high corner and subsequently subsampled to 0.060 s by TGS personnel prior to being written to disk. The work presented in this manuscript only analyzes the Z- and P-component data; however, we note that the horizontal components are likely useful for complementary identification of different wave modes and phenomena contained within the data set.

After inspecting the recordings from each receiver, we identified a 35-day period when all receivers were concurrently recording. We also discovered that some receivers either were deployed later or ended recording earlier than the vast majority of the survey in that time window. In addition, we noted several nodes that had unidentifiable polarity changes; while these may have been corrected in the active-source survey, it is challenging to identify the corrections needed with ambient records. Due to these uncertainties, we removed the 38 affected OBNs from our analysis, resulting in 2712 OBNs being used for the ensuing experiments.

During the OBN acquisition period an active-source survey was being conducted by three source acquisition vessels, each using two air-gun arrays. There were approximately 2.06 million air-gun shots at nominally 20 s intervals, which were designed to generate frequencies to as low as 1.7 Hz. Because we are predominantly examining energy in the sub-1.0 Hz frequency bands, we did not expect significant overlap from the active sources in these bandpassed and subsampled recordings.

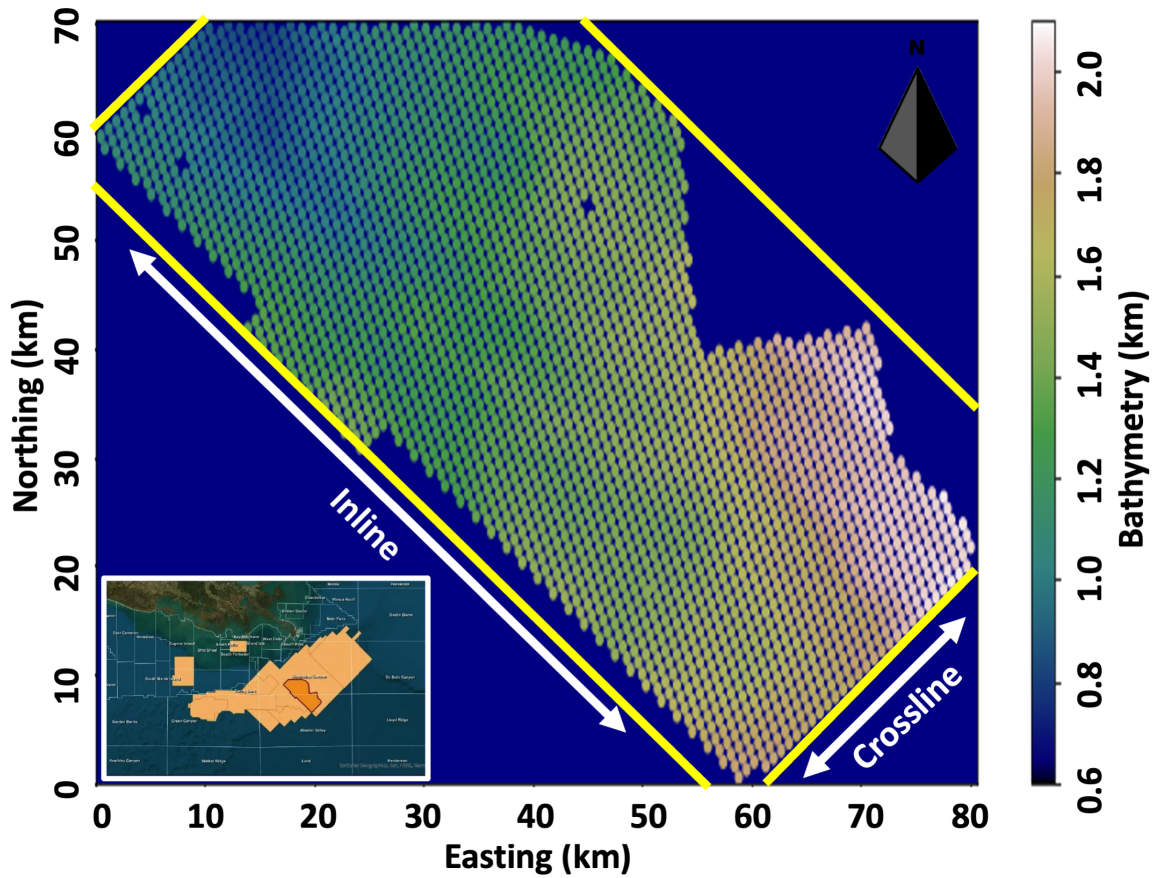


Figure 1. Amendment OBN deployment geometry with individual stations colour-coded by seafloor bathymetry. The overall deployment covered an approximately 80 km by 40 km area. Images below are presented in an inline-crossline coordinate system rotated approximately 45° clockwise from geographic north that is given by yellow bounding box with directions indicated by the annotated white arrows. The inset map (courtesy of TGS) shows location of the survey area in the GoM, where the southern Louisiana coastline is shown toward the top.

150 After analyzing the ambient data and identifying ambient wavefield characteristics that sug-
 151 gested subsurface influence, we were provided with a P-wave velocity (V_P) model by TGS. This
 152 FWI model was derived from the higher-frequency active-source P-component data using acoustic
 153 FWI (Huang et al. 2020). TGS personnel subsequently downsampled the high-resolution model to
 154 a uniform 0.1 km spacing in all three dimensions. No velocity information was used in processing
 155 the ambient records or calculating the VSGs; however, we use this information for independent
 156 corroboration of observed data features.

3 PRESTACK AMBIENT PROCESSING WORKFLOW

This section presents the prestack ambient wavefield data workflow applied to the low-frequency Amendment OBN data set. We note that there are numerous approaches and open-source packages that can be used for ambient wavefield processing (see, e.g., Prieto et al. 2011; Lecocq et al. 2014; Jiang et al. 2020). Here, we follow the approach outlined in Girard & Shragge (2020) that is applied within the open-source Madagascar data processing framework (Fomel et al. 2013). This section highlights the four main workflow steps applied in this study: (1) time-header synchronization; (2) data window selection; (3) time debursting; and (4) frequency debursting. The applied workflow has been largely adapted with only minor changes to that presented in Girard & Shragge (2020); readers interested in additional procedural details are referred to this work.

3.1 Time-header synchronization

When using long-time seismic recordings for interferometry, it is imperative that the timing of each sensor is consistent throughout the survey because the interferometry process will otherwise generate incorrect correlation-lag information (and consequently incoherent VSGs). Because acquisition information indicated that the clock errors were less than a single 0.06 s time sample, the raw data were not corrected for clock drift. Therefore, the first step was to ensure that each trace has identical start and stop times to facilitate correlation traces and recovery of wavefront propagating across the array with the correct correlation lag for each receiver pair. However, some nodes prematurely stopped recording (due to battery or other mechanical failure) and were therefore removed from the data set in favor of a longer global recording window. Because this affected less than 0.5% of the nodes, we decided that excluding them would not be detrimental to the interferometric analysis.

We ensured that each OBN record was windowed to the same length with the same origin time by examining the header information; fortunately this required no modification from the original records. The data set was organized in 30-minute windows upon delivery, a structure that was maintained when generating “common-ambient-window” gathers (i.e., the equivalent of a common shot gather in active-source seismic acquisition). This window duration was deemed

184 sufficient to recover ultra-low frequency information when generating VSGs and was therefore
185 left unchanged during the ambient prestack data processing.

186 **3.2 Data window selection**

187 Not all ambient seismic data are valuable for identifying low-frequency information through in-
188 terferometry analysis (see, e.g., Prieto et al. 2011). Some records will be dominated by singular
189 large-amplitude events (e.g., earthquakes, OBN deployment ROVs) that dominate the interfero-
190 metric stacking process. In other cases, individual OBN stations will be influenced by nearby
191 energy sources that are too faint to be detected at other receiver stations and are thus not correlat-
192 able across the array and offer no value for interferometric analysis. Therefore, it is important to
193 judiciously select a set of optimal windows with “appropriate statistics” such that calculated VSGs
194 are more likely to highlight weak ambient energy propagating through the earth.

195 This work approaches data selection of ambient records through a multi-step procedure that is
196 due to the non-stationary nature of unwanted signals contained within the data volumes. For ex-
197 ample, an impulsive high-amplitude event compared to a moderate-amplitude but longer-duration
198 event can have different effects on the overall interferometric stack quality. Here, we use a se-
199 lection process that aims to eliminate statistically anomalous high-amplitude windows (Nakata et
200 al. 2015). The window-selection step involves removing windows with residual high root-mean-
201 square (rms) energy amplitudes (Issa et al. 2017). To do so, we computed short- versus long-term
202 averages (McEvelly & Majer 1982) to prioritize high-energy windows for removal. Based on this
203 information, we defined a global magnitude threshold (70%) using the pressure component from
204 every OBN (though this could be done using any individual or combination of components) for
205 eliminating windows with abnormally large rms energy values. We do this because of calendar
206 variations in environmental conditions (e.g., effects of severe weather disturbances, distal earth-
207 quakes) that cause some windows to exhibit relatively high unwanted signal levels. The resulting
208 recording time used for the remainder of the experiment is 588.0 hours or equally 24.5 days.

209 **3.3 Time debursting**

210 There are different scenarios that can cause individual channels to have a strong “burst-like” energy
211 disturbance on ambient recordings, and including these unwanted energy sources in long-time
212 stacks can skew the statistical convergence of interferometric analyses. Here, we remove burst-
213 like data from individual seismic time-series data using an L_1 iteratively reduced least-squares
214 (IRLS) debursting approach (Claerbout 2014). (We term this ‘time debursting’ to differentiate
215 it from the ‘frequency debursting’ procedure discussed below.) This time-debursting operation
216 addresses residual high-energy events remaining after performing the data masking and window
217 selection steps. To apply this filter, we calculate the envelope for each trace individually and choose
218 a preservation threshold (70%) based on the window rms energy and the highest residual spike
219 amplitude remaining after the data selection step. Waveforms with magnitudes greater than this
220 threshold are reduced to the selected threshold value without hard clipping, while those with lower
221 amplitudes are unaffected by the debursting process. We assert that this data conditioning approach
222 is a judicious alternative to hard clipping or sign-bit normalization, which can introduce frequency-
223 domain artifacts via discontinuous particle accelerations.

224 **3.4 Frequency debursting**

225 Other types of unwanted signals can cause frequency-domain spiking when they are stacked over
226 long periods (e.g., electromechanical signal of repeated turning lights on and off). To address these
227 types of unwanted signals sources, we apply a similar process to the previous processing step
228 to mitigate strong monochromatic (or narrow-band) energy, which manifests as ringing in time-
229 domain VSGs. To do this, we modify the time-debursting method of Claerbout (2014) to operate
230 on Fourier magnitude spectra while leaving the corresponding phase spectra untouched. This filter
231 again down-weights monochromatic energy of significantly greater levels than the background
232 magnitude spectrum to a user-specified level. We then combine the untouched phase and filtered
233 magnitude spectra and apply an inverse Fourier transform to complete the ambient prestack data
234 processing workflow. By removing strong, localized frequency-domain energy we aim to minimize

235 coherent monochromatic noise in processed time-domain ambient data while preserving phase-
236 component information important for reconstructing empirical Green's function kinematics.

237 There are a number of different approaches that can be used to address spike-like structure
238 in frequency-domain data. While notch filtering is commonly applied to remove various types
239 of monochromatic noise in active-source seismic experiments (Linville 1994), designing non-
240 stationary notch filters for each window and characteristic frequency makes automation challeng-
241 ing if not impractical. In addition, notch filters can introduce artifacts by affecting phase informa-
242 tion. Our approach differs from notch filtering in that it neither requires prior knowledge of the
243 frequency structure nor designs a suite of filters to remove energy at specific peak frequencies.
244 This frequency-debursting technique leaves filtered spectral magnitudes at levels commensurate
245 with those of nearby Fourier components, which is unlikely to be true with notch filtering applica-
246 tions. The parameter defining how much to filter spiky amplitudes was chosen through parameter
247 testing during processing on representative VSG examples.

248 **3.5 Processing QC check**

249 To visualize the effects of the processing sequence detailed above, Figure 2 presents representative
250 spectrograms taken immediately after the selection process (Figure 2a) and after applying the full
251 data processing workflow (Figure 2b) for a station located in the middle of the Amendment OBN
252 array. The first spectrogram exhibits strong vertical banding with otherwise limited energy below
253 0.4 Hz and between 2600-4000 minutes. Relative to the first spectrogram, the fully processed
254 version now clearly shows significant sub-1.0 Hz energy with coherent energy appearing to near
255 0 Hz. The first 1300 and final 1400 minutes of representative recording time also show "Dirac
256 combing" effects that manifest as horizontal lines between 0.05-0.20 Hz (see Discussion section
257 below).

258 **3.6 Cross-coherence Interferometry**

259 After data processing, there are several available techniques of interferometry available to recon-
260 struct VSGs from ambient seismic wavefields. Aki (1957) introduces the concept of using auto-

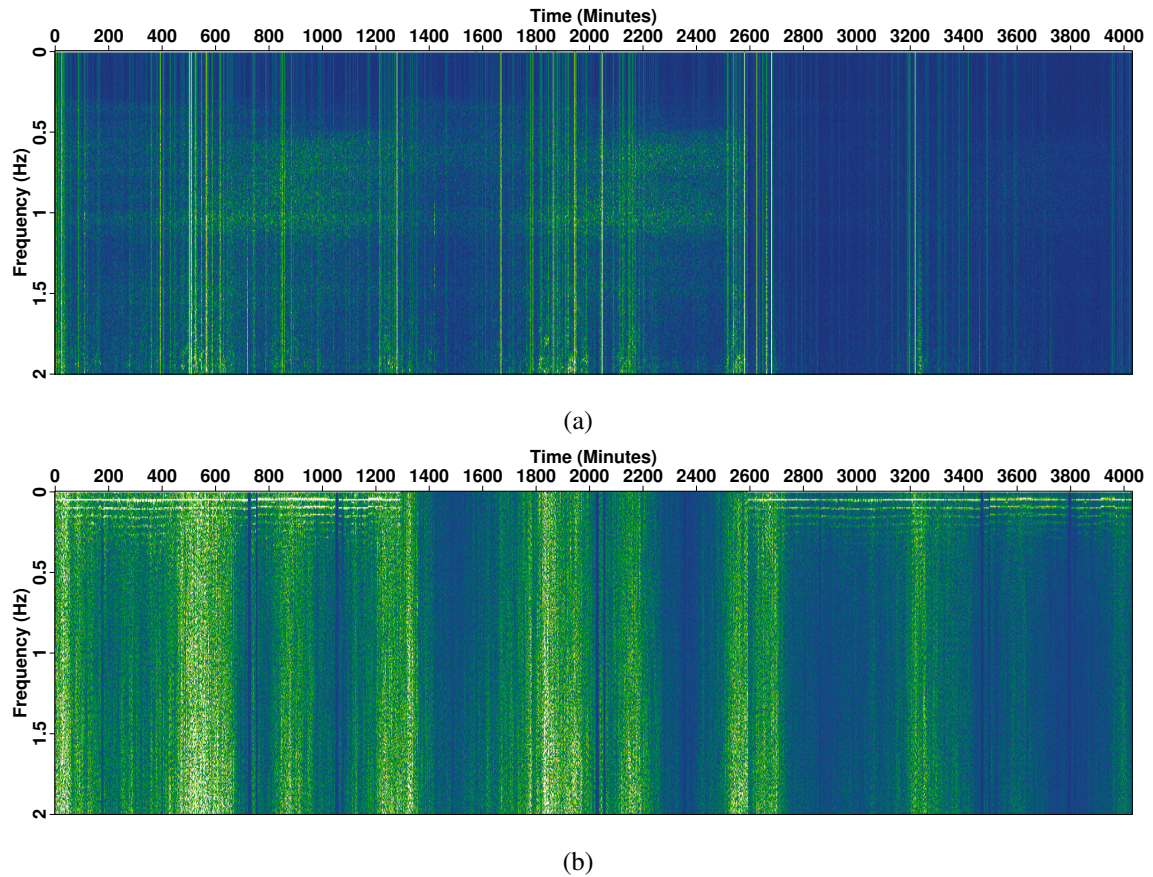


Figure 2. (a) Representative 67-hour spectrogram computed from raw data after rejecting 30% of the highest rms energy windows for a station located in the middle of the Amendment Phase 1 OBN array (see Figure 1). (b) Spectrogram of the same data after applying the full preprocessing workflow that shows clearly visible sub-1.0 Hz energy.

261 correlations to identify wave-mode characteristics to analyse stationary waves in the Earth. Claer-
 262 bout (1968) arguably develops a precursor to seismic interferometry for a 1-D earth as a method to
 263 retrieve a seismic impulse response (Green’s function) by cross-correlating wavefields measured
 264 at two different receiver points, thereby creating a “virtual” source at the location of the first re-
 265 ceiver. Interferometric VSGs also can be generated with an improved cross-correlation-plus-stack
 266 workflow that extracts the empirical Green’s function response (Wapenaar 2004). The spectral bal-
 267 ance of a VSG can be improved through deconvolution (Wapenaar et al. 2011) or cross-coherence
 268 (Nakata et al. 2011) processing, which allows for a choice of smaller regularization parameter and
 269 remains stable because amplitude is not explicitly preserved (Prieto et al. 2009).

270 We calculate VSGs using a CUDA-based code for cross-coherence interferometric calcula-
 271 tions (Girard et al. 2023) that first transfers wavefield traces for each window from the CPU to the
 272 GPU, computes the forward Fourier transforms over the time axis, and then calculates the (sym-
 273 metric) cross-coherence VSG I_{ij} contribution between the i th and j th OBN component, U_i and
 274 U_j , according to:

$$275 I_{ij}(\mathbf{x}_A, \mathbf{x}_B, \omega) = \sum_{m=1}^M \frac{\overline{U_i(\mathbf{x}_A, \omega, m)} U_j(\mathbf{x}_B, \omega, m)}{|U_i(\mathbf{x}_A, \omega, m)| |U_j(\mathbf{x}_B, \omega, m)| + \epsilon^2}, \quad i, j = P, Z \quad (1)$$

276 where $\overline{U_i}$ represents the complex conjugate of the wavefield U_i ; $\mathbf{x}_A = (x_A, y_A)$ and $\mathbf{x}_B = (x_B, y_B)$
 277 are the coordinates of OBN stations A and B ; ω is angular frequency; m is the window index; M is
 278 the total number of windows; the wavefield magnitude is given by $|U_i| = \sqrt{(\Re(U_i))^2 + (\Im(U_i))^2}$;
 279 and $\epsilon = 0.05$ is a small positive real constant (i.e., after trace normalization) used for spectral-
 280 whitening operation (Wapenaar et al. 2011). The outer sum of the cross-coherence calculation
 281 stacks each window after calculating $I_{ij}(\mathbf{x}_A, \mathbf{x}_B, \omega)$. The GPU code then applies an inverse Fourier
 282 transform over the frequency axis to recover the $I_{ij}(\mathbf{x}_A, \mathbf{x}_B, \tau)$, where variable τ is the two-sided
 283 temporal correlation lag. Compared to other preprocessing workflow steps, the cross-coherence
 284 calculation is extremely fast, taking approximately 12 minutes on a single NVidia V100 GPU card
 285 to compute a single VSG at one virtual-source location for all 1176 windows each with 30,000
 286 samples and 2712 receivers.

287 4 RESULTS AND OBSERVATIONS

288 We next present the results of applying the prestack ambient processing and interferometry work-
 289 flow to generate the output VSG volumes. We first discuss the numerical procedure for generating
 290 wavefield propagation images and then analyze the frequency composition and wave propaga-
 291 tion embedded within the Z- and P-component VSG volumes. Next, we highlight observations
 292 of signal waveforms with an approximately 20 s periodicity asserted to be associated with the
 293 same periodicity of active-source air-gun source interval. Finally, we illustrate observations of
 294 strong surface-wave scattering from subsurface velocity structure interpreted to be associated with
 295 a shallow salt body.

4.1 Gridding and image generation

After interferometric processing, the resulting VSGs were output at each OBN location (see Figure 1) as a 3D data cube with the following axes: time lag τ , and the virtual shot \mathbf{x}_A and receiver \mathbf{x}_B locations. To minimize unused space in the following images, figures appearing below are presented in an inline-crossline “deployment” coordinate system $\mathbf{x} = [x_i, x_c]$ that is rotated approximately 45° clockwise from geographic north. The first visualization step involved bandpassing individual traces to different frequency bands of interest for the ensuing frequency-decomposition analysis. We then used the OBN geometry to grid the narrow-band 3-D VSG volume for each virtual shot at 0.5 km intervals in both the inline and crossline direction. These intervals were approximately half the mean (staggered) station spacing, which allowed for more accurate spatial nearest-neighbor binning though at the cost of introducing “holes” within the gridded 3-D volumes. For visualization purposes, we next applied uniaxial triangular convolutional smoothing along the inline and crossline directions to infill holes and reduce binning-based high spatial-wavenumber content prior to applying sinc interpolation to spatially map the data to a uniformly sampled 0.25 km grid. While this procedure proved sufficient for figure generation, more advanced spatial data gridding and interpolation techniques is recommended before using the interpolated 3-D VSG data for any follow-on imaging and inversion work.

4.2 Vertical-component VSG analysis

The first set of examples presents a frequency-decomposition analysis of the Z-component VSGs. Figure 3 shows a representative Z-component VSG time slice extracted at time lag $\tau = 10.0$ s from an OBN located at inline and crossline coordinates $[x_i, x_c] = [46.0, 16.5]$ km. This volume has been filtered in eight frequency bands within the $10^{-2} - 10^0$ Hz range of interest to highlight different wave phenomena (Shen et al. 2012). Overall, the panels exhibit a remarkable coherency across the illustrated spectral range.

Figure 3a presents the wavefield estimate in lowest frequency band between 0.008-0.04 Hz and shows a near azimuthally symmetric waveforms about the OBN location to a radial distance of about 35 km. Progressing through the next two frequency bands of 0.008-0.075 Hz (Figure 3b)

323 and 0.01-0.15 Hz (Figure 3c), the radial expression of the VSG data reduces to respectively about
 324 30 km and 25 km. The next three frequency bands of 0.075-0.275 Hz (Figure 3d), 0.17-0.45 Hz
 325 (Figure 3e) and 0.30-0.65 Hz (Figure 3f) exhibit increasingly compact waveforms. The final two
 326 frequency bands of 0.35-0.83 Hz (Figure 3g) and 0.50-1.00 Hz (Figure 3h) continue this trend,
 327 though are getting close to the limit where spatial aliasing becomes evident due to the OBN sam-
 328 pling geometry. Overall, the frequency decomposition analysis suggests that the processed long-
 329 time VSGs contain coherent information at distances approaching a minimum of 40 km over the
 330 $10^{-2} - 10^0$ Hz frequency range.

331 Figure 4 presents an example of wave propagation contained within a VSG volume. The eight
 332 wavefield snapshots are extracted from the 0.35-0.825 Hz frequency band shown in Figure 3g and
 333 start at 4.0 s (Figure 4a) and increase with 3.0 s increments to a 25.0 s maximum (Figure 4h). The
 334 wavefront expands nearly circularly with increasing lag time; however, various outward “kinks”
 335 suggest faster propagation in some locations likely due to the presence of shallow salt bodies.

336 4.3 Pressure-component VSG analysis

337 Figure 5 presents a complementary analysis to that shown in Figure 3, but now for the P-component
 338 data at 10.0 s for a VSG located at $[x_i, x_c] = [58.0, 19.5]$ km. The panels again show eight different
 339 narrow frequency bands between 0.008-1.0 Hz. Similar to the Z-component data examples, the
 340 waveforms appear coherent in all bands with the lowest frequency bands exhibiting a broader
 341 expression than at higher frequencies. In addition, the wavefield is starting to appear spatially
 342 aliased in Figure 5h. Finally, we note that Figures 5f-h show secondary scattering radiating outward
 343 from a point centred at $[x_i, x_c] = [65.0, 16.8]$ km. These observations are discussed further in
 344 Section 4.5 below.

345 Figure 6 presents a wave-propagation example in the 0.35-0.85 Hz frequency band extracted
 346 from P-component VSG data at the same VSG location as in Figure 5. Figure 6a-h respectively
 347 present wavefield time slices starting at 4.0 s at 3.0 s increments to a maximum of 25.0 s. We
 348 note that as the VSG propagates, the wavefield especially toward low inline coordinates becomes

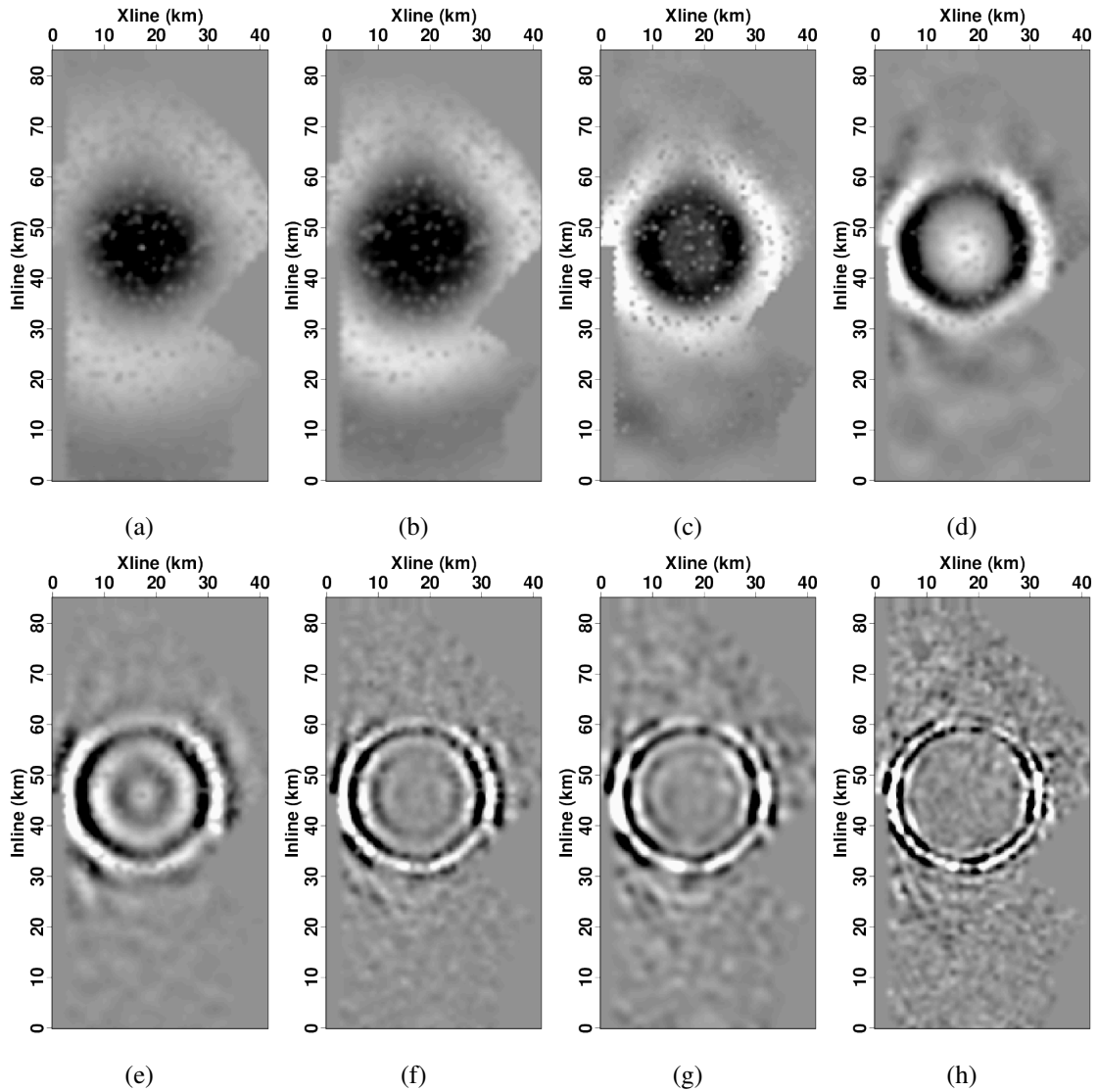


Figure 3. Representative Z-component VSG time slice extracted at 10.0 s from an OBN station located at $[x_i, x_c] = [46.0, 16.5]$ km filtered to eight different frequency bands. (a) 0.008-0.04 Hz. (b) 0.008-0.075 Hz. (c) 0.01-0.15 Hz. (d) 0.075-0.275 Hz. (e) 0.17-0.475 Hz. (f) 0.30-0.65 Hz. (g) 0.35-0.825 Hz. (h) 0.50-1.0 Hz.

349 increasingly dispersive. Finally, Figure 6b shows the onset of the aforementioned surface-wave

350 scattering that is more evident in Figures 6c-e.

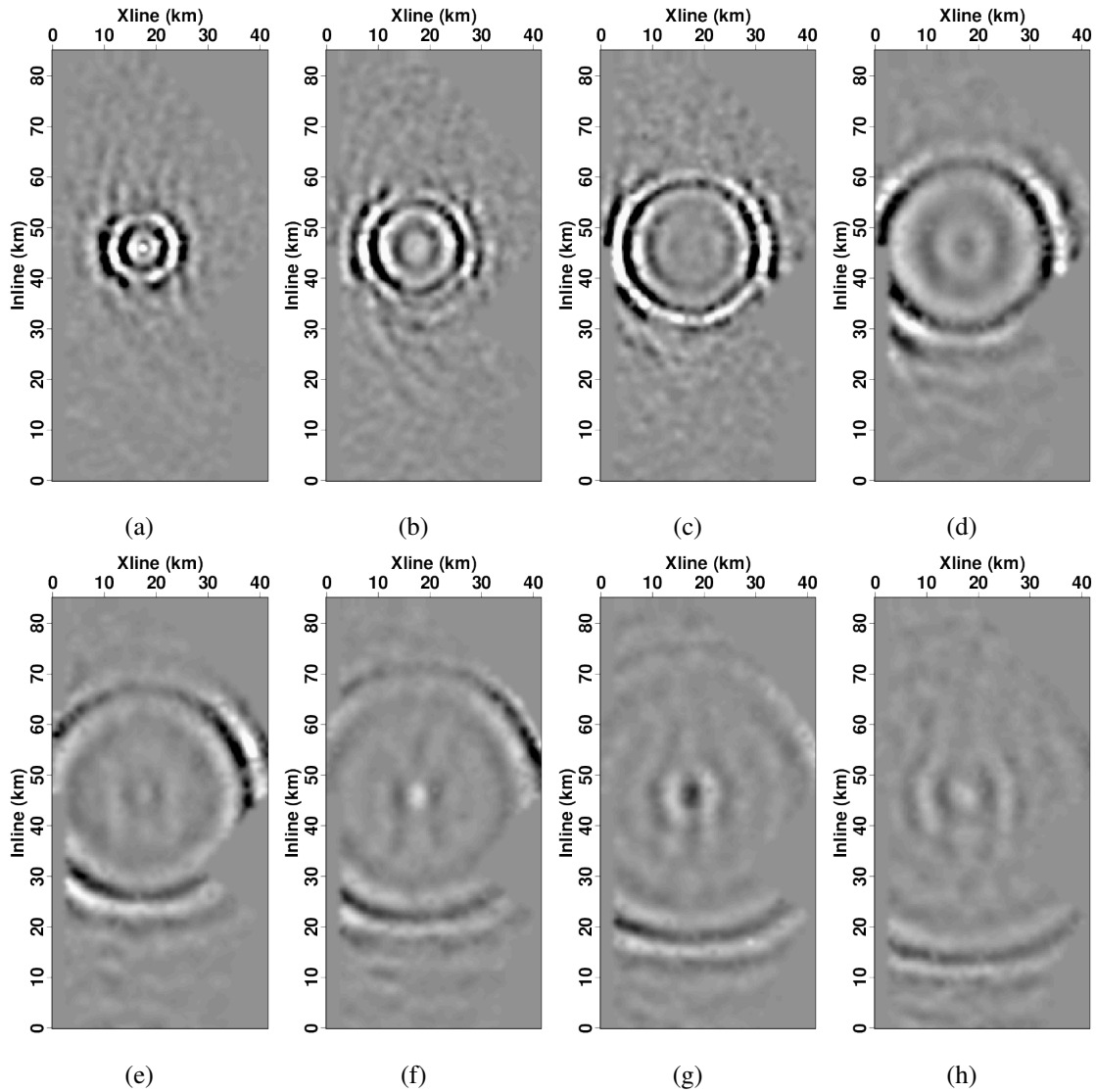


Figure 4. Z-component VSG filtered between 0.35-0.825 Hz extracted from an OBN located at $[x_i, x_c] = [46.0, 16.5]$ km for eight different time lags. (a) 4.0 s. (b) 7.0 (s). (c) 10.0 s. (d) 13.0 s. (e) 16.0 s. (f) 19.0 s. (g) 22.0 s. (h) 25.0 s.

351 4.4 VSG Spatial Heterogeneity

352 The broad radial symmetry of the observed VSGs wavefields suggests that an alternate way to
 353 visualize and analyze the observed waveforms is to bin the 3-D VSGs using the following coordi-
 354 nates: correlation lag τ , source-receiver absolute offset r , and source-receiver azimuth ϕ . One can
 355 then compute the average stack over the azimuthal coordinate ϕ to extract a 2-D mean radial $\tau - r$
 356 VSG panel. The main purpose of the stacking is thus two-fold: (1) improve the overall signal-to-

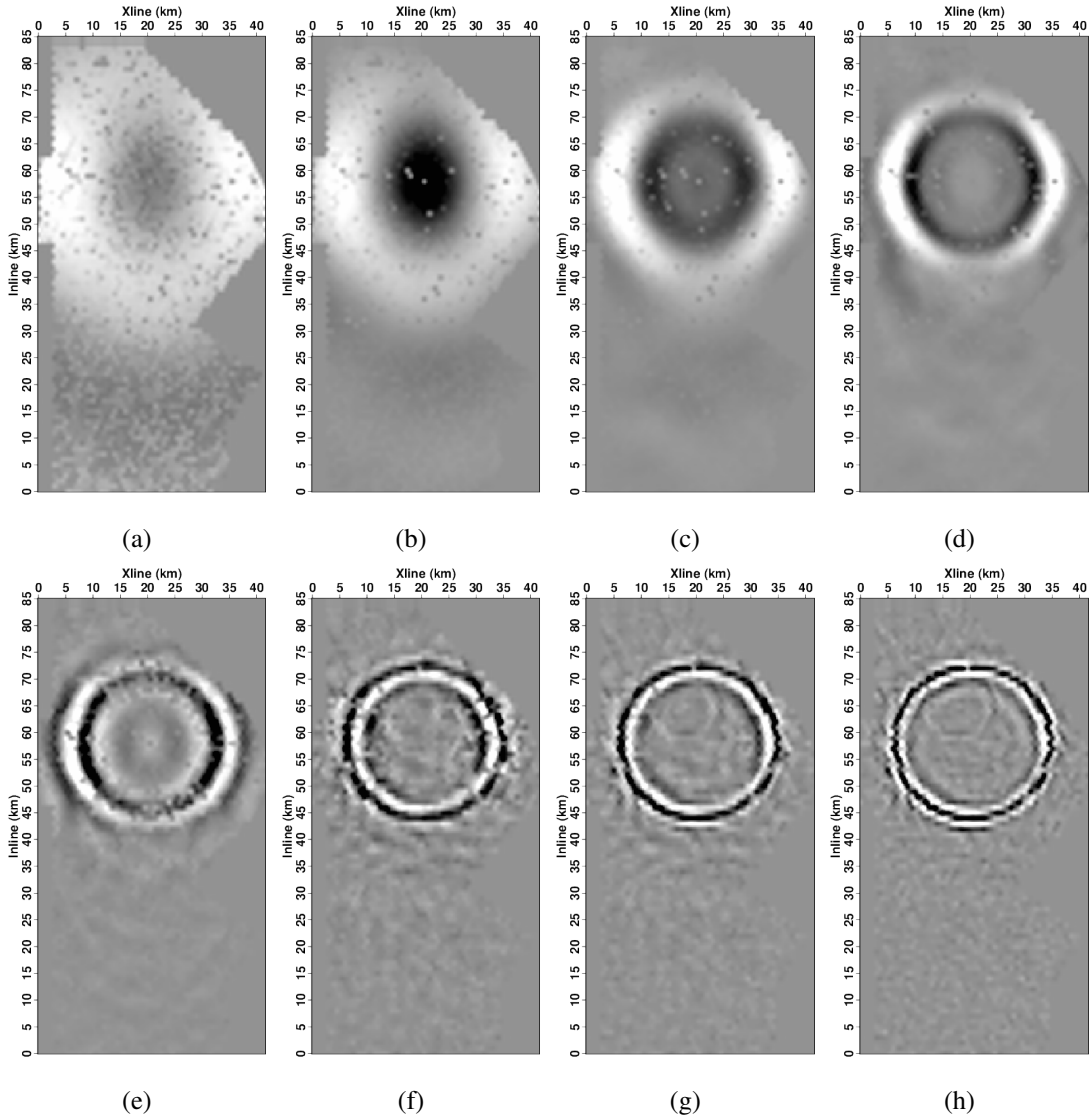


Figure 5. Representative P-component time slice extracted at 10.0 s correlation lag from an OBN located at coordinate $[x_i, x_c] = [58.0, 19.5]$ filtered to different frequency bands. (a) 0.008-0.04 Hz. (b) 0.008-0.075 Hz. (c) 0.01-0.15 Hz. (d) 0.075-0.275 Hz. (e) 0.17-0.475 Hz. (f) 0.30-0.65 Hz. (g) 0.35-0.825 Hz. (h) 0.50-1.0 Hz.

357 noise ratio of the VSG observations; and (2) reduce the data dimensionality from 3-D to 2-D for
 358 more effective visual presentation.

359 Figure 7 presents representative Z-component radial $\tau - r$ panels for a VSG from a deep-water
 360 OBN located at $[x_i, x_c] = [3.0, 17.0]$ km and 1723 m water depth that have been bandpassed to
 361 the same frequency ranges as those presented in Figure 3 and Figure 5. The panels depict coherent

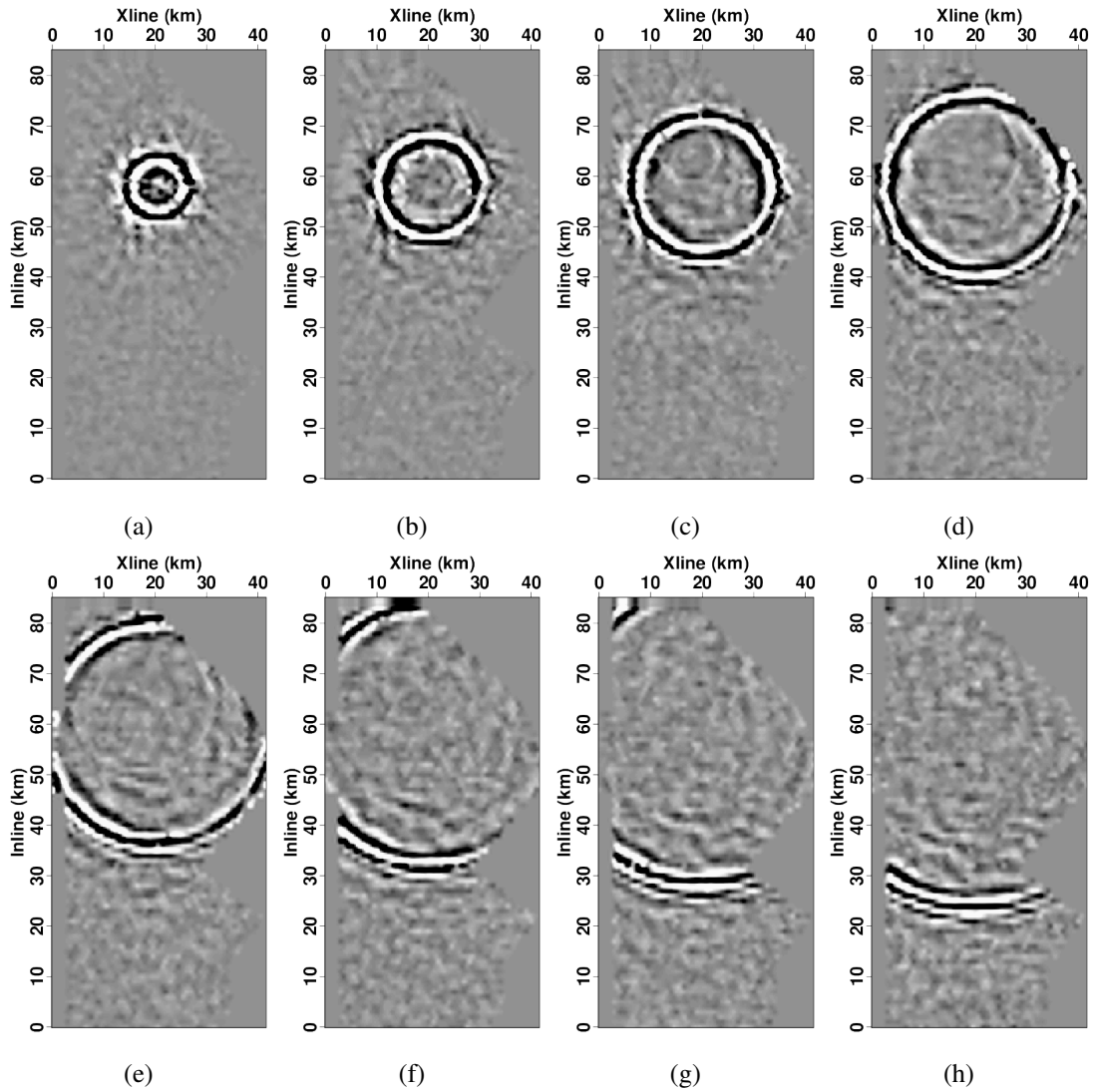


Figure 6. P-component VSG filtered between 0.35-0.83 Hz extracted from an OBN located at coordinate $[x_i, x_c] = [58.0, 19.5]$ for different time lags. (a) 4.0 s. (b) 7.0 (s). (c) 10.0 s. (d) 13.0 s. (e) 16.0 s. (f) 19.0 s. (g) 22.0 s. (h) 25.0 s.

362 energy over almost the full 80 km of absolute offset range. Interestingly, Figures 7b-7e show
 363 a clear multiple-like pattern repeating at approximately 20 s intervals. The other panels exhibit
 364 weak-to-no repetition, suggesting that the signal band predominantly falls between 0.05-0.5 Hz.
 365 This observation is further analyzed in Section 4.4 below. A further observation in Figures 7f-7h is
 366 that the dominant arrivals start to develop “shingling” behavior, as indicated by the discontinuous
 367 surface-wave arrivals. This behavior is most prominently observed between 0.4-1.0 Hz.

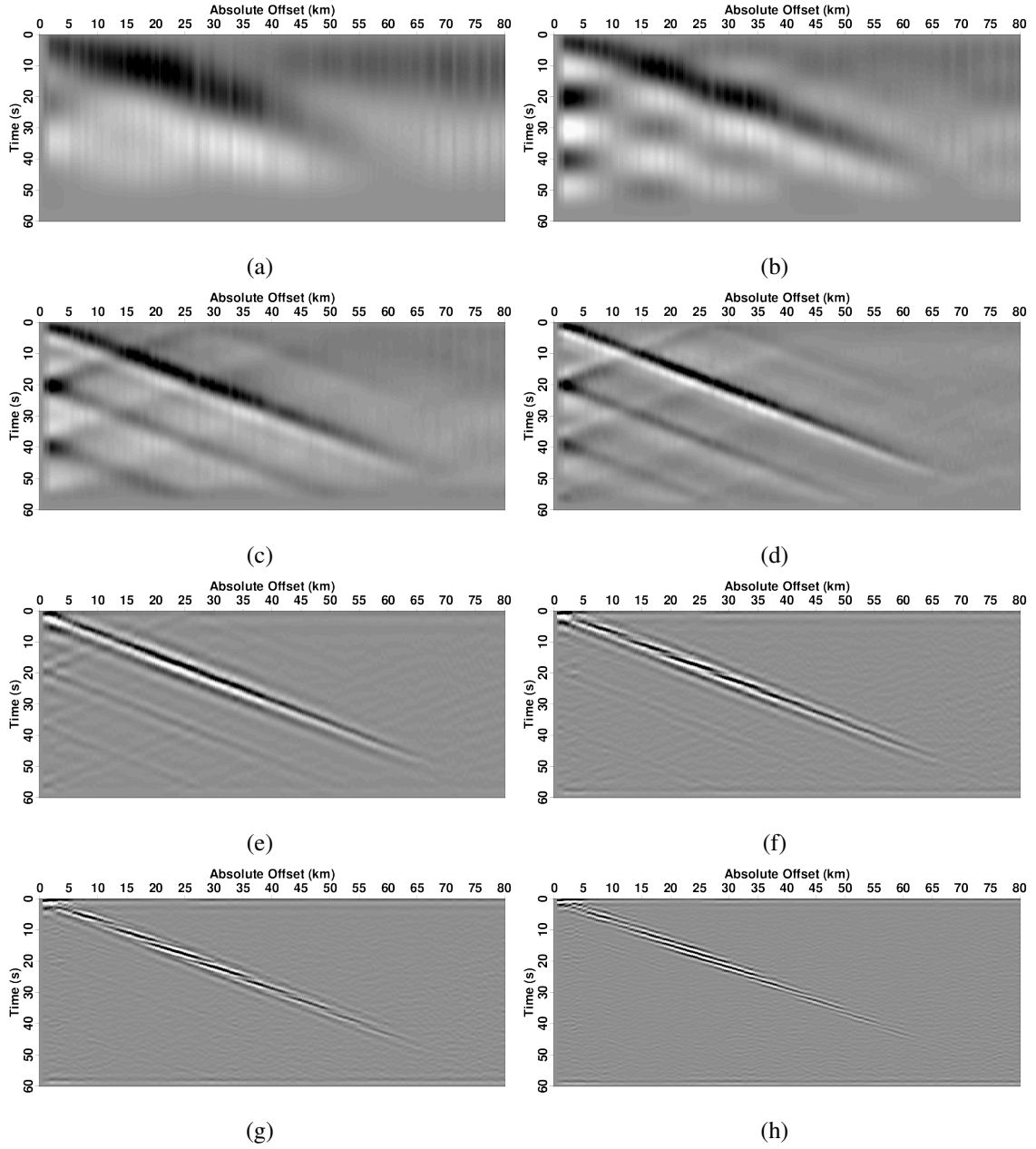


Figure 7. Z-component absolute offset r and correlation time τ panel after stacking over all azimuths for a VSG from a deepwater OBN located at coordinate $[x_i, x_c] = [3.0, 17.0]$ km and at 1723 m water depth, filtered in eight different frequency bands. (a) 0.008-0.04 Hz. (b) 0.008-0.075 Hz. (c) 0.01-0.15 Hz. (d) 0.075-0.275 Hz. (e) 0.17-0.475 Hz. (f) 0.30-0.65 Hz. (g) 0.35-0.825 Hz. (h) 0.50-1.0 Hz.

368 Figure 8 presents the same absolute-offset stack but for P-component observations. Again,
 369 propagated energy is visible over nearly the full 80 km of absolute offset. Repetitive signals with
 370 a 20 s recurrence interval are visible, though only in Figures 8b-8e. There is also a notable change
 371 in the character of the observed waveforms between Figures 8e and 8f suggesting a transition
 372 between different wave-mode types between 0.3-0.4 Hz. The waveforms at frequencies higher
 373 than this transition range clearly exhibit dispersive behavior.

374 Given the bathymetric variations observed in the survey area, an interesting question is whether
 375 there are visible differences between VSG volumes for OBNs situated in deep versus shallow wa-
 376 ter. To address this question, Figures 9 and 10 present results for OBN stations located in deep and
 377 shallow water, respectively. Figure 9a presents a phase-velocity-frequency (PVF) plot calculated
 378 using Z-component VSG data for a deepwater OBN located at coordinate $[x_i, x_c] = [3.0, 17.0]$ km
 379 and at 1.72 km water depth. The image depicts two distinct wave modes with different characteris-
 380 tics. The first mode in frequency bands between 0.15-0.45 Hz exhibits a 1.38 km/s phase velocity
 381 that increases moderately at about 0.08 Hz to 1.40 km/s. Figure 9b illustrates the Z-component
 382 $r - \tau$ panel filtered to a 0.05-0.28 Hz frequency band, which depicts a strong linear arrival at the
 383 expected 1.4 km/s moveout. The second mode falling between 0.45-1.25 Hz is significantly more
 384 dispersive and exhibits phase velocities in the 2.4-1.7 km/s range. Figure 9c, which presents the
 385 Z-component $r - \tau$ panel filtered between 0.35-0.83 Hz, shows waveforms with a similar 1.4 km/s
 386 moveout as the interpreted surface waves in Figure 9b; however, there is a “shingling” effect com-
 387 prised of waveforms with shallower dips indicating elements of dispersive wave propagation that
 388 are in agreement with PVF-visualized moveouts. Figure 9d presents the P-component PVF plot
 389 for the same OBN station and again depicts two types of waveforms. The first is interpreted as
 390 a low-frequency surface wave between 0.05-0.25 Hz that is significantly lower magnitude in the
 391 P-component relative to Z-component recordings. Unlike in Figure 9a, there is no evidence for
 392 surface waves in P-component waveforms between 0.25-0.45 Hz in this image. Figure 9e presents
 393 the P-component $r - \tau$ panel filtered in the 0.05-0.28 Hz frequency band. The main arrival is very
 394 similar to that observed on the Z component (Figure 9b). The second set of waveforms are inter-
 395 preted as a guided P-wave package with a dominant lower modes and perhaps as many as three

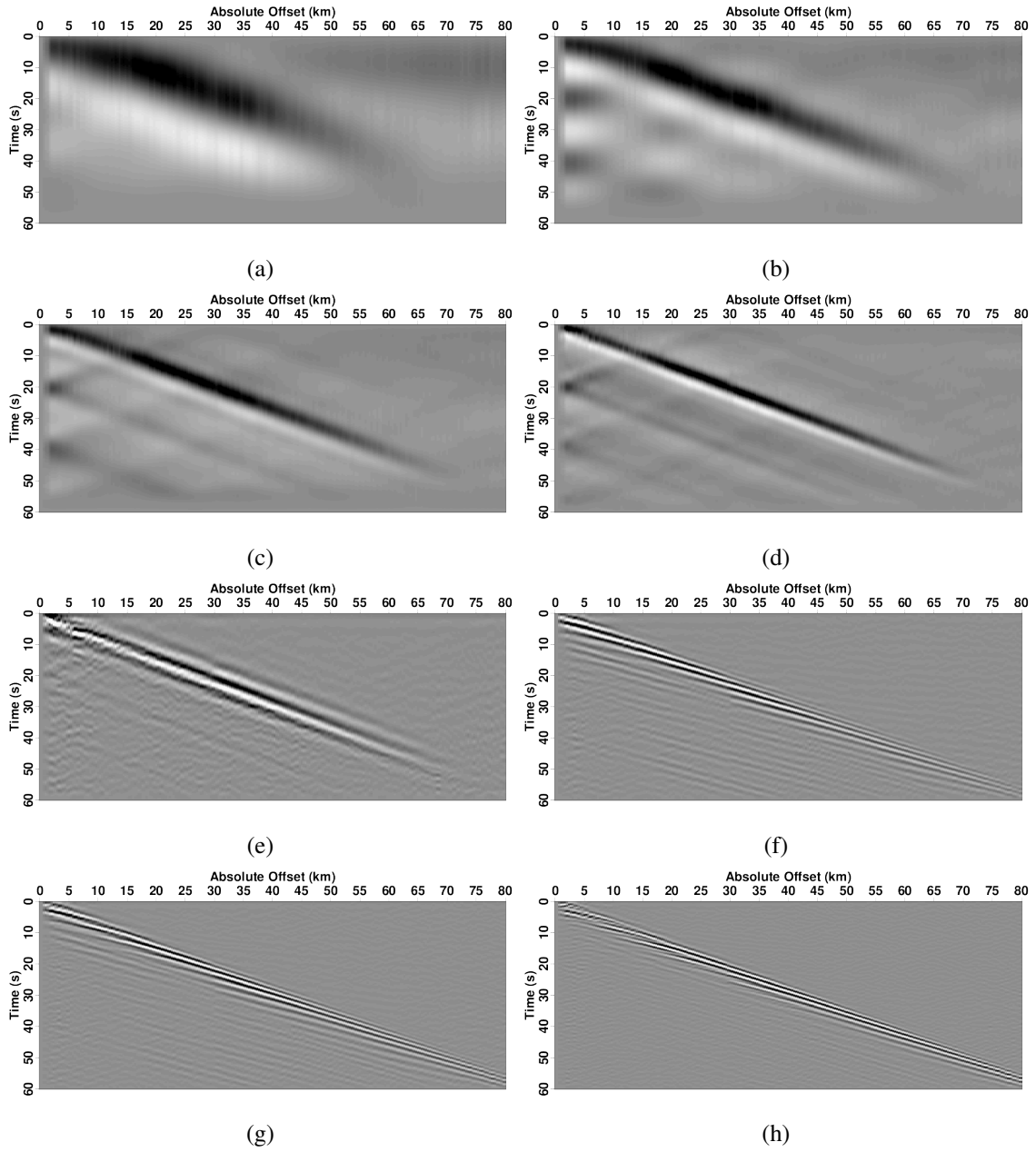


Figure 8. P-component $r - \tau$ panel after stacking over all azimuths for a VSG at the same location as in Figure 7, filtered in eight frequency bands. (a) 0.008-0.04 Hz. (b) 0.008-0.075 Hz. (c) 0.01-0.15 Hz. (d) 0.075-0.275 Hz. (e) 0.17-0.475 Hz. (f) 0.30-0.65 Hz. (g) 0.35-0.825 Hz. (h) 0.50-1.0 Hz.

396 visible higher-order modes. These guided compressional waveforms are generated by multiply re-
 397 flected/refracted waves trapped within the water column (Hokstad 2004; Shi et al. 2023). Figure 9f

398 presents the P-component $r - \tau$ panel filtered between 0.35-0.83 Hz. The main arrival is distinct
 399 from that observed on the Z component (Figure 9c) and exhibits dispersive mode interference.

400 We repeat the analysis presented in Figure 9 but for data acquired on a shallow-water OBN
 401 station located at coordinate $[x_i, x_c] = [79.0, 14.0]$ m at 0.96 km water depth (see Figure 10).
 402 Compared to the PVF plot in Figure 9a, the Z-component PVF panel presented in Figure 10a
 403 highlights an interpreted surface wave mode largely falling within the same frequency band. The
 404 relatively reduced definition may be due to the shorter 45 km distance over which coherent arrival
 405 is observed (Figure 10b) as well as more complex, shallow bathymetry to the northwest of the
 406 array. We also note that the dispersive waveforms clearly evident in Figure 9c are now largely
 407 absent from Figure 10c. The P-component PVF panel in Figure 10d again depicts a low-frequency
 408 wave mode at 1.4 km/s in the 0.05-0.25 Hz band, though at lower magnitudes and for shorter
 409 absolute offsets than that observed in the deep-water example (Figure 10e). In addition, unlike the
 410 deepwater example, only a single interpreted guided P-wave mode is visible in Figure 10d.

411 **4.5 Air-gun source contributions**

412 One observation discussed above is the presence of multiple-like energy in VSG data recurring
 413 at approximately 20 s intervals (see, e.g., Figures 7b-f and 8b-f). This energy is present in both
 414 shallow- and deep-water settings and thus is unlikely associated with bathymetric variations. Thus,
 415 an interesting question is what is the cause of these repeating 20 s periodic signals? To investigate
 416 this question, we examine the available tabulated active-source shot-timing records. First, we parse
 417 out sequential shot-timing data for each of two air-gun arrays on the three boats used to acquired
 418 active-source data. We then compute the time difference between shots by differencing the succes-
 419 sive shot times. The resulting times are then stacked and binned at 1.0 s intervals to generate the
 420 shot-delay histogram presented in Figure 11. Based on these data, we observe that the dominant
 421 shot interval falls between 18-22 s with 20 s having the highest recurrence count. Overall, we are
 422 not aware of any additional anthropogenic or natural signal occurring with such a dominant 20 s
 423 periodicity.

424 The implication of this observation is that the air-gun array is responsible for generating the

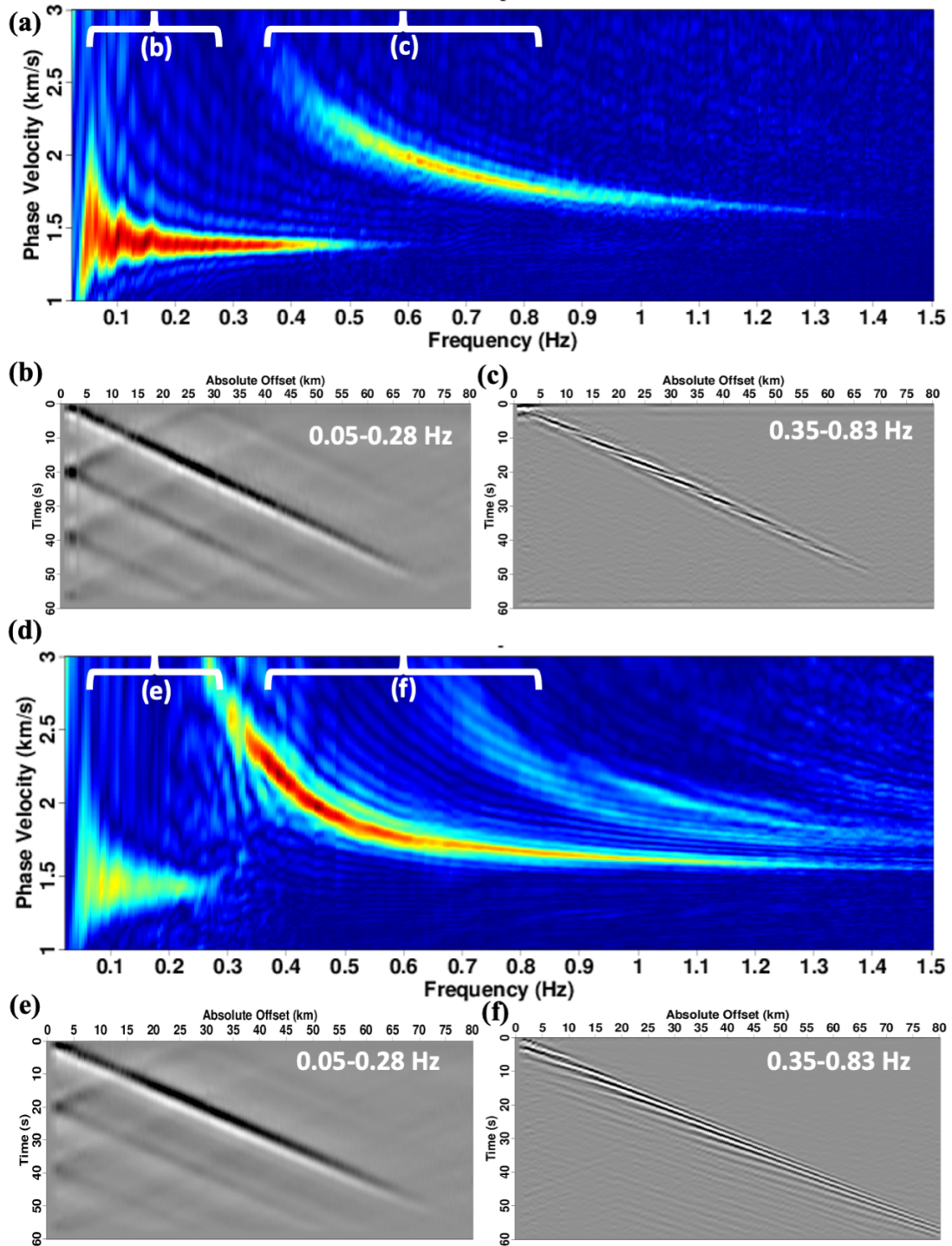


Figure 9. Waveform analysis using Z- and P-component $r-\tau$ panels acquired on a deep-water OBN located at $[x_i, x_c] = [3.0, 17.0]$ km and 1723 m water depth (same as in Figure 7). (a) Z-component phase-velocity-frequency (PVF) panel showing two distinct wave types in the (b) 0.05-0.35 Hz and (c) 0.35-1.25 Hz frequency bands. (d) P-component PVF panel showing two distinct wave types interpreted to be in the (e) 0.05-0.35 Hz and (f) 0.35-1.25 Hz frequency bands. A 0.75 time-gain has been applied to the $r-\tau$ panels for visualization purposes.

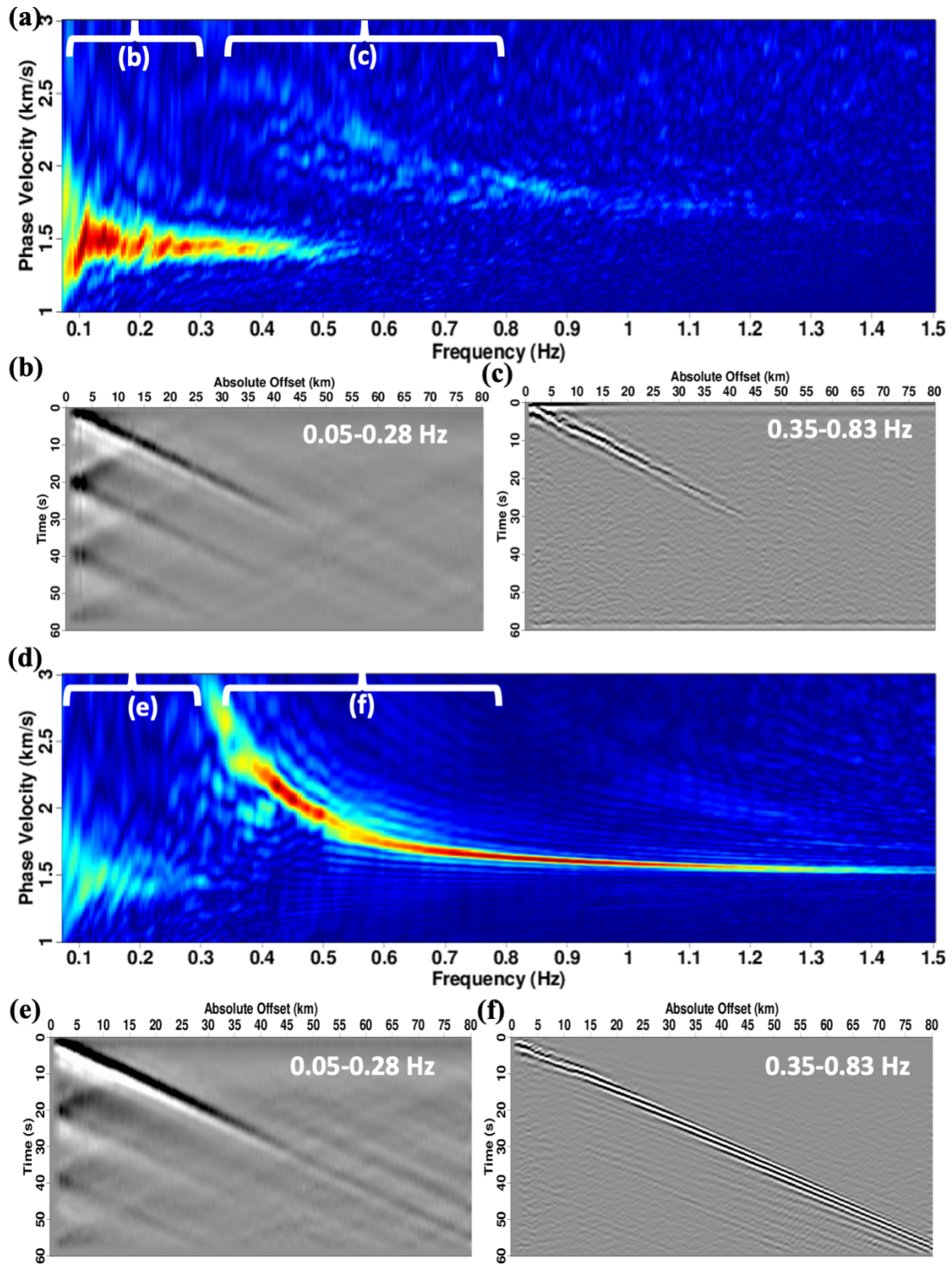


Figure 10. Waveform analysis using Z- and P-component $r-\tau$ panels acquired on a shallower-water OBN at coordinate $[x_i, x_c] = [79.0, 14.0]$ km at 957 m water depth. (a) Z-component PVF panel showing two distinct wave types in the (b) 0.05-0.35 Hz and (c) 0.35-1.25 Hz frequency bands. (d) P-component PVF panel showing two distinct wave types interpreted to be (e) 0.05-0.35 Hz and (f) 0.35-1.25 Hz frequency bands. A 0.75 time-gain has been applied to the $r-\tau$ panels for visualization purposes.

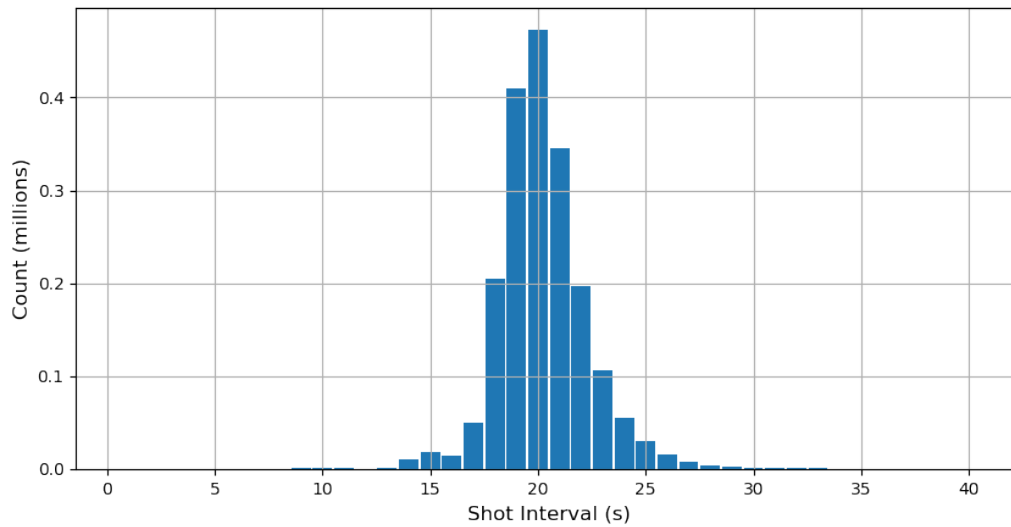


Figure 11. Shot recurrence interval extracted from available records showing the dominant 18-22 s peak, which is consistent with the “multiple-like” signal repetition observed at 20 s in Figures 9b and e and 10b and e.

425 interpreted surface waves within the 0.01-0.30 Hz frequency band. Previous research examines
 426 the generation of lower-frequency (i.e., 1-5 Hz) surface waves (specifically Scholte waves) excited
 427 by explosions or vertical impact sources on or near the seafloor and recorded by ocean-bottom
 428 seismometers (e.g., Essen 1980; Schirmer 1980; Rauch 1986; Gimpel 1987; Stoll 1991; Ewing et
 429 al. 1992; Stoll & Bautista 1994; Krone 1997). Other work demonstrates that air-gun sources in
 430 relatively shallow-water settings can generate surface waves (particularly Scholte waves) of mea-
 431 surable amplitude though at frequencies generally above 2 Hz (e.g., Ritzwoller & Levshin 2002;
 432 Klein 2003; Bohlen et al. 2004; Kugler et al. 2007). However, we are unaware of any previous
 433 reports of surface waves generated by air-gun arrays in the 0.01-0.30 Hz frequency band. We
 434 stress that, for any individual active-source shot record, the generated surface-wave energy would
 435 be below the noise floor; however, the consistency of air-gun waveforms over the approximately
 436 2.06 million shots, with the majority of shots falling outside any given interferometric pair, com-
 437 bined with the cross-coherence plus stack processing enables surface-wave energy to become the
 438 dominant observable signal in VSGs in this frequency band.

439 4.6 Surface-wave scattering

440 A further interesting observation is the surface-wave scattering noted above that persists across a
 441 wide range of VSGs and suggests the presence of a point-like diffraction scatterer located in the
 442 vicinity of $[x_i, x_c] = [65.0, 16.8]$ km. Figure 12 presents representative time-slice panels extracted
 443 from VSGs in the frequency band (0.58-0.83 Hz) for eight different VSG locations approximately
 444 situated at the four cardinal and four intercardinal orientations. The centre panel shows the V_P
 445 model extracted at 2.5 km depth, where the blue and red colours represent sediments and salt, re-
 446 spectively. Each VSG panel shows both portions of the clipped outward-propagating direct surface
 447 wave as well as a scattered wavefield emanating from the scattered location. The crosshairs in the
 448 panels indicate the approximate centre of the circular scattering. To better illustrate the subsurface
 449 feature potentially generating the scattering, Figure 13 presents a cube view showing the inline
 450 and crossline V_P cross-sections at $[x_i, x_c] = [65.0, 16.8]$ km. This observation suggests that the
 451 scattering may be related to a nearby shallow salt “pinnacle” located approximately 1.0 km below
 452 the seafloor.

453 To investigate whether surface-wave scattering in the 0.5-0.8 Hz frequency range might be
 454 expected at 1.0-2.0 km depths, we model theoretical 1-D Rayleigh-wave sensitivity kernels using
 455 the *disba* software package (Luu 2021) for the generic sediment V_P and V_S profiles shown in
 456 14a. Figure 14b presents 0.2-2.0 Hz Rayleigh-wave sensitivity kernels scaled by the period for
 457 visualization purposes. The green 0.5 Hz curve shows that the sensitivity peak is at approximately
 458 0.5 km depth and ranges from a null at the seafloor to near zero by 2.5 km depth. Similarly, the
 459 orange 1.0 Hz curve peaks at 0.25 km depth and ranges between the null at 0 km and is nearly
 460 zero by 1.5 km depth. Thus, the assertion that surface-wave scattering from a salt body located
 461 at approximately 1.0 km below the seafloor is not inconsistent with the Rayleigh-wave sensitivity
 462 kernels at the given frequency range.

463 5 DISCUSSION

464 This section addresses a number of key questions posed in the Introduction: (1) can coherent
 465 waveforms be recovered by seismic interferometry on arrays with station spacing of approximately

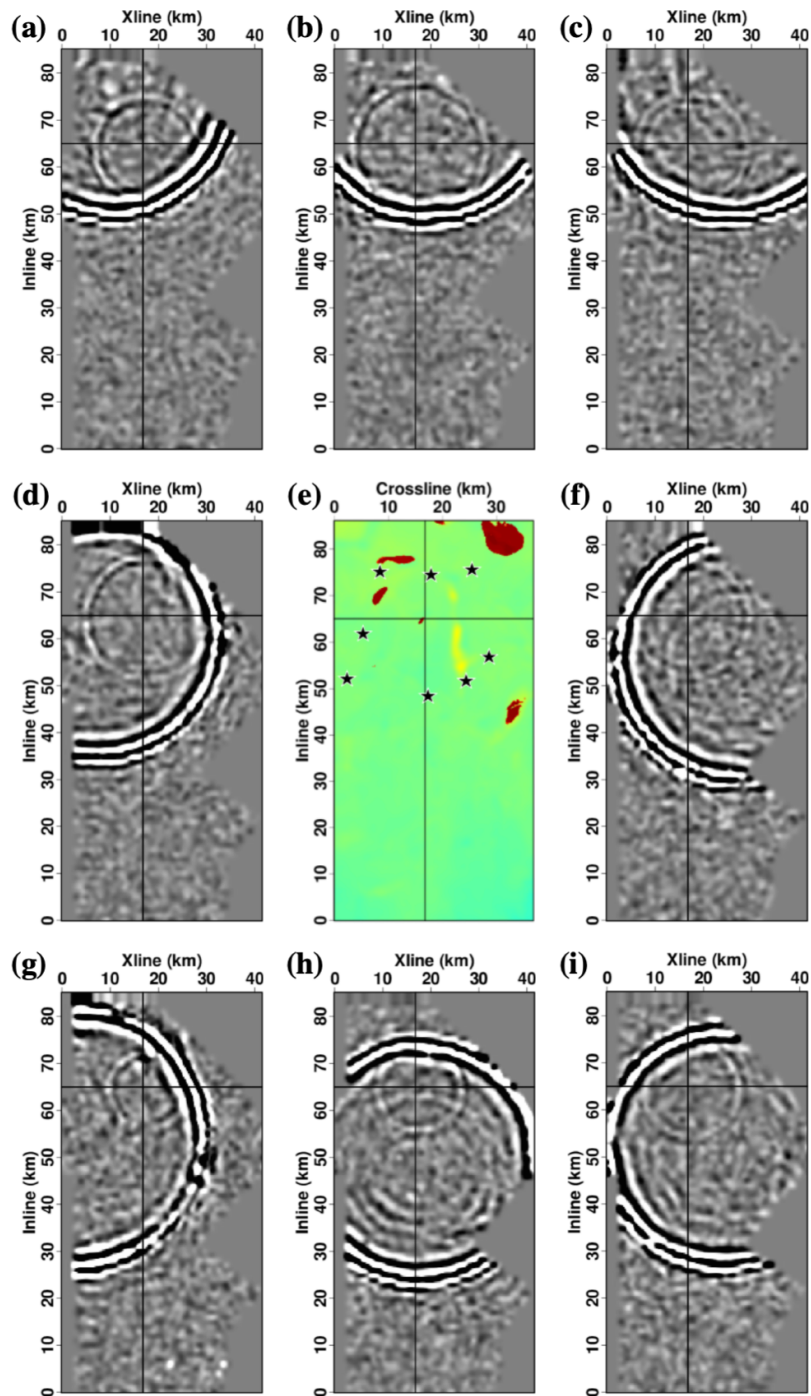


Figure 12. (a)-(d) and (f)-(i) Representative examples of surface-wave scattering extracted from eight VSG volumes between 0.5-1.0 Hz calculated at the locations indicated by the black stars in (e). (e) Velocity slice extracted at 2.3 km depth below the surface. The cross-hairs in the eight wavefield panels indicate the approximate centres of scattered events, which are consistent with the location of shallow salt pinnacle in (e) and illustrated in Figure 13.

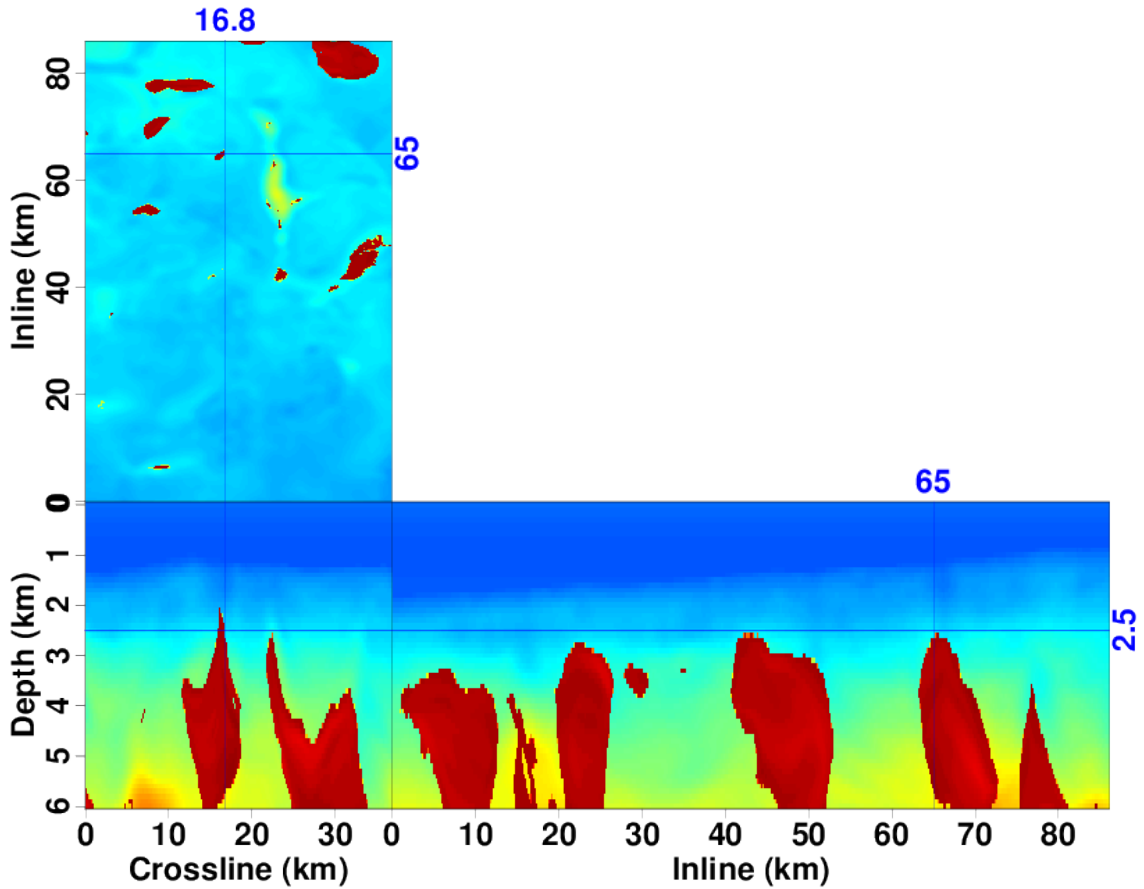


Figure 13. 3-D V_P model independently reconstructed from active-source Amendment Phase 1 OBN survey data. The cross-hair corresponds to the same locations of those illustrated in Figure 12.

466 1 km or larger? (2) can conventional 4-C OBN instruments recover usable ultra-low frequency
 467 content? (3) does ultra-low-frequency ambient wavefield energy coherently propagate across larger
 468 arrays? and (4) how do these observations affect the prospectus for low-frequency elastic model
 469 building?

470 **5.1 VSGs and OBN array sparseness considerations**

471 The sensor spacings used in typical exploration-scale OBN array deployments (e.g., 300-500 m,
 472 see Table 1) usually are sufficient for non-aliased spatial sampling of low-frequency wavefields
 473 like those observed in the VSG data presented in this experiment. The Amendment Phase 1 OBN
 474 survey, though considered to be a sparse array when deployed at 1 km nominal spacing, remains

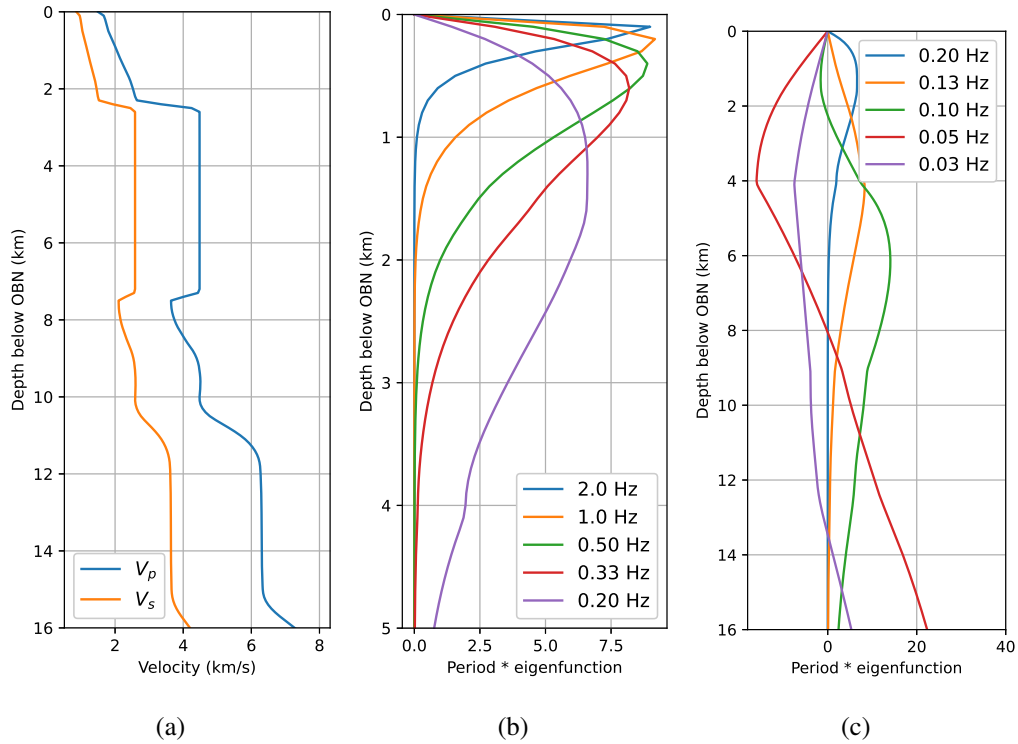


Figure 14. Period-weighted Rayleigh-wave sensitivity kernels. (a) 1-D V_P and V_S models used in the calculation respectively extracted and derived from the subsampled active-source Amendment V_P model. Computed sensitivity kernels for the (b) 0.2-2.0 Hz and (c) 0.013-0.10 Hz frequency ranges. Note that the curves are scaled by the period for visualization purposes, and the depth range in (b) is reduced compared to (c) to more clearly emphasize the shallower sensitivities at higher frequencies.

475 sufficient to recover long-wavelength wavefield information. For ultra-low-frequency data used to
 476 create the Amendment VSGs, we still effectively oversample surface waves for wavelengths rang-
 477 ing from ten kilometers to a few tens of kilometers. However, at frequencies nearing 1.0 Hz (and
 478 as low as 0.75 Hz for 1.4 km/s surface waves), this array nears the Nyquist sampling criteria of two
 479 samples per wavelength required for unaliased recovery of the corresponding spatial wavelengths.

480 For geological scenarios where surface-wave phase velocities are significantly lower than those
 481 shown herein (i.e., 1.4 km/s), one could easily encounter spatial aliasing at frequencies around
 482 1.0 Hz. For example, de Ridder & Biondi (2015) presents an example at the Ekofisk field in the
 483 North Sea where observed surface-wave phase velocities fall between 0.4-0.6 km/s for frequen-
 484 cies ranging between 1.3-0.4 Hz. Thus, station sampling around 0.3-0.5 km would be needed to

adequately sample the shorter wavelength surface-wave contributions in that particular geological environment.

Overall, we consider OBN spatial sampling may be an important factor when aiming to use VSG wavefield information falling near the spatial Nyquist value for FWI model building activities.

5.2 VSGs and geophone/hydrophone corner frequency

One of the more surprising observations is that the geophone and hydrophone sensors were able to recover coherent wavefield information two-to-three decades below the stated cut-off frequencies - especially considering that no frequency-dependent instrument phase and magnitude corrections were applied as part of this processing. We speculate that there are two key associated factors: the use of interferometric cross-coherence processing and the statistics of long-term stacking. First, we note that the interferometric process uses cross-coherence plus stacking in the m th of M windows of a wavefield recorded at station A with magnitude $A_m = A_m(\mathbf{x}_A, \omega)$ and phase $\phi_m^A = \phi_m^A(\mathbf{x}_A, \omega)$ [i.e., $U_i(\mathbf{x}_A, \omega, m) = A_m e^{i\phi_m^A}$] with that at station B with magnitude $B_m = B_m(\mathbf{x}_B, \omega)$ and phase $\phi_m^B = \phi_m^B(\mathbf{x}_B, \omega)$ [i.e., $U_j(\mathbf{x}_B, \omega, m) = B_m e^{i\phi_m^B}$]. To investigate the phase component of the interferometric processing, we insert these expressions into the numerator of equation 1 to obtain:

$$\begin{aligned} I_{num}(\mathbf{x}_A, \mathbf{x}_B, \omega) &= \sum_{m=1}^M \overline{A_m e^{i\phi_m^A}} B_m e^{i\phi_m^B} \\ &= \sum_{m=1}^M \overline{A_m} B_m e^{i(\phi_m^B - \phi_m^A)}. \end{aligned} \quad (2)$$

where the phase difference is due to evaluation of the complex conjugate. Let us now consider a model where the phase component of each signal window is represented by the sum of three elements: (1) the true window-independent wavefield phases $\psi_A(\omega)$ and $\psi_B(\omega)$; (2) the deterministic instrument phase error $\gamma = \gamma(\omega)$; and (3) random zero-mean noise terms ϵ_m^A and ϵ_m^B usually assumed to arise due to a random Gaussian process. Inserting $\phi_m^A = \psi_A + \gamma + \epsilon_m^A$ and $\phi_m^B = \psi_B + \gamma + \epsilon_m^B$ into equation 2 yields

$$I_{num}(\omega, \mathbf{x}_A, \mathbf{x}_B) = \sum_{m=1}^M \overline{A_m e^{i(\psi_A + \gamma + \epsilon_m^A)}} B_m e^{i(\psi_B + \gamma + \epsilon_m^B)}$$

$$= \sum_{m=1}^M \overline{A_m B_m} e^{i(\psi_B - \psi_A + \epsilon_m^B - \epsilon_m^A)}, \quad (3)$$

507 which has no explicit dependence on instrument phase error γ_ϕ . Moreover, as M approaches
 508 “large” (e.g., over a 35-day acquisition period), one assumes that the net contribution of the zero-
 509 mean Gaussian error difference $\epsilon_m^B - \epsilon_m^A$ ideally becomes negligible through repeated stacking.
 510 Thus, we expect the phase response of calculated VSG data to be sufficiently accurate due to the
 511 use of the long-term interferometric cross-coherence-plus-stacking process - even at frequencies
 512 much lower than the stated sensing element cutoff values.

513 We note that a similar analysis on wavefield magnitude spectra is made challenging by the
 514 myriad preprocessing steps applied before and during VSG generation. In fact, one of the reasons
 515 why we performed narrow-band filtering of VSG volumes in this work is due to the significant
 516 variations in magnitude spectra. Specifically, VSG data between $10^{-3} - 10^{-1}$ Hz decades are
 517 significantly weaker than those in the $10^{-1} - 10^0$ Hz decade. Thus, we stress the importance
 518 of performing narrow-band frequency decomposition when analyzing broadband ambient VSG
 519 energy contributions due to the complexities of handling the variable amplitude scales.

520 **5.3 Ultra-low-frequency ambient wavefield coherence**

521 A similarly notable finding from the VSGs for the Amendment data set is a demonstration of
 522 coherent wavefields propagating at ultra-low frequencies with very long associated wavelengths.
 523 This is largely due to the much larger aperture of the Amendment array (80 km by 40 km) than
 524 those listed in Table 1, which makes it possible to identify propagating surface waves with wave-
 525 lengths in the tens of kilometer range. In addition to larger aperture, the frequencies recorded
 526 in the VSG volumes likely are generated by active-source air-gun excitation with a regular 20 s
 527 shooting interval (or equivalently 0.05 Hz). While ocean waves and swell are known to generate
 528 energy that transfers into the subsurface in the $10^{-3} - 10^0$ Hz band and is generally recognized as
 529 a key source of observed low-frequency energy in VSGs, this work presents strong evidence for
 530 measured active-source contributions at these low frequencies generated by 2.06 million repeated
 531 air-gun excitations.

5.4 Model Building Prospectus

The effective surface-wave propagation velocity may be considered as a weighted average of the elastic model properties over the depth range where the associated sensitivity kernel exhibits meaningful values (Ekström et al. 2009). At the ultra-low-frequencies shown in Figure 14c (i.e., 0.03-0.20 Hz), Rayleigh waves are sensitive to depths exceeding 10 km. This suggests that the surface-wave modes observed in Amendment VSG data in the 0.05-0.20 Hz range are likely useful for constraining the long-wavelength 3-D elastic model components at the 0-10 km depth range most important for seismic exploration. In addition, any secondary scatterers present in the various frequency bands of observation (see, e.g., Figure 12) could be used to identify locations of anomalous short-wavelength geological formations (e.g., salt pinnacles) that can be used to further constrain elastic model building analyses.

A corresponding challenge in elastic model building, though, is the need to correctly identify the different types of wave modes present in the data. Initial coupled acoustic-elastic modeling efforts indicate that a wide variety of factors (e.g., source characteristics; observation frequency; bathymetry; presence of guided P-wave modes; background S-wave velocity gradients; and presence or absence of shallow, fast salt canopy of variable thickness) combine to contribute to a large range of possible forward modeling outcomes. While surface-wave-mode (in particular Rayleigh and Scholte) sensitivities are indeed related (Bagheri et al. 2015), they do exhibit distinct characteristics that if incorrectly identified can lead to erroneous inversion-based velocity-model results. A further confirmatory forward modeling effort is currently under way to assist with wave-mode identification; however, this topic remains beyond the scope of the current work.

6 CONCLUSIONS

This paper presents the results of an ambient wavefield study using low- and ultra-low-frequency data acquired on the large-scale Gulf of Mexico Amendment Phase 1 OBN array. We demonstrate that combining prestack ambient data preprocessing and cross-coherence interferometry workflows leads to the recovery of coherent surface-wave arrivals from as low as 0.008 Hz to about 1.0 Hz. Stacking VSG data over azimuths leads to lag-offset panels that show strong coherency

559 of wavefield arrivals to distances up to (and likely exceeding) 80 km. Phase-velocity-frequency
560 plots suggest the presence of interpreted low-frequency surface wave-mode arrivals below 0.4 Hz
561 in both the Z- and P-component data. We highlight the presence of surface-wave scattering from
562 a shallow salt-body pinnacle that appears in numerous VSGs located at numerous azimuths with
563 respect to the scattering point. Finally, we present evidence that air-gun energy stacked over long
564 periods is measurable on OBN arrays at sub-0.3 Hz frequencies. This assertion is based on the
565 observed 20 s periodicity of waveforms, which is consistent with the mean 20 s active-source
566 shooting interval. This suggests that the dominant generator of “ambient” wavefield energy during
567 the Amendment ambient data acquisition is likely the excitation of active-source air-gun arrays
568 rather than naturally occurring microseism energy. Overall, these findings suggest that ultra-low-
569 frequency seismic energy acquired on standard OBN hardware, after appropriate preprocessing,
570 can generate high-quality, coherent, and interpretable VSGs volumes. Moreover, the resulting VSG
571 waveforms show a broad sensitivity to subsurface velocity structure and, thus, may provide a po-
572 tential pathway forward for generating elastic starting models for FWI analyses.

573 **ACKNOWLEDGMENTS**

574 To be completed at a later date.

575 **Data availability**

576 Data associated with this research are confidential and cannot be released.

577 **REFERENCES**

- 578 Aki, K., 1957, Space and time spectra of stationary stochastic waves, with special reference to mi-
579 crotremors: *Bulletin of the Earthquake Research Institute*, **35**, 415-456.
- 580 Bagheri, A., Greenhalgh, S., Khojasteh, A., and Rahimian, M., 2015, Dispersion of Rayleigh, Scholte,
581 Stoneley and Love waves in a model consisting of a liquid layer overlying a two-layer transversely
582 isotropic solid medium: *Geophys. J Int.*, **203**(1), 195–212.
- 583 Bromirski, P., Duennebieer, F., and Stephen, R., 2005. Mid-ocean microseisms: *Geochemistry, Geophysics,*
584 *and Geosystems*, **6**(4), Q04009.

- 585 Bussat, B., and Kugler, S., 2011. Offshore ambient-noise surface-wave tomography above 0.1 Hz and its
586 applications: *The Leading Edge*, **30**, 514–524.
- 587 Bohlen, T., Kugler, S., Klein, G., and Theilen, F., 2004. 1.5D inversion of lateral variation of Scholte-wave
588 dispersion: *Geophysics*, **69**(2), 330–344.
- 589 Carcione, J.M., Bagaini, C., Ba, J., Wang, E., and Vesnaver, A., 2018. Waves at fluid–solid interfaces: ex-
590 plicit versus implicit formulation of the boundary condition: *Geophysical Journal International*, **215**(1),
591 3–48.
- 592 Claerbout, J.F., 1968. Synthesis of a layered medium from its acoustic transmission response: *Geophysics*,
593 **34**(2), 264–269.
- 594 Claerbout, J.F., 2014. *Geophysical Image Estimation by Example*: LULU Press.
- 595 de Ridder, S., and Dellinger, J., 2011. Ambient seismic noise eikonal tomography for near-surface imaging
596 at Valhall: *The Leading Edge*, **30**, 506–512.
- 597 de Ridder, S.A.L., and Biondi, B.L., 2015. Ambient seismic noise tomography at Ekofisk: *Geophysics*,
598 **80**(6), B167–B176.
- 599 de Ridder, S.A.L., and Maddison, J.R., 2018. Full wavefield inversion of ambient seismic noise, *Geophys.*
600 *J Int.*, **215**(2), 1215–1230.
- 601 Ekström, G., Abers, G. A., and Webb, S. C., 2009. Determination of surface-wave phase velocities across
602 USArray from noise and Aki’s spectral formulation, *Geophys. Res. Lett.*, **36**(18), L18301.
- 603 Essen, H.-H., 1980, Model computations for low-velocity surface waves on marine sediments, in Ku-
604 perman, W. A., and Jensen, B., Eds., *Bottom-interacting ocean acoustics: NATO Conference Series 4*,
605 299–305.
- 606 Ewing, J., Carter, J., Sutton, G.-H., and Barstow, N., 1992. Shallow water sediment properties derived
607 from high-frequency shear and interface waves: *Journal of Geophysical Research*, **97**(B4), 4739–4762
- 608 Fomel, S., Sava, P., Vlad, I., Liu, Y., and Bashkardin, V., 2013. Madagascar: open-source software project
609 for multidimensional data analysis and reproducible computational experiments. *Journal of Open Re-*
610 *search Software*, **1**, e8.
- 611 Gimpel, P., 1987. *Marineflachseismische Untersuchungen in der Kieler Bucht unter besonderer*
612 *Berücksichtigung von Scherwellenmessungen*: PhD Dissertation, Universität Kiel.
- 613 Girard A.J., Shragge, J., and Olofsson, B., 2023. Low-frequency ambient ocean-bottom node surface-wave
614 seismology: A Gulf of Mexico case history, *Geophysics*, **88**(1), B21–B32.
- 615 Girard, A.J. and Shragge, J., 2020. Automated processing strategies for ambient seismic data: *Geophysical*
616 *Prospecting*, **68**(1): 293–312.
- 617 Hokstad K., 2004, Nonlinear and dispersive acoustic wave propagation, *Geophysics* **69**(3), 840–848.
- 618 Huang, Y., Mao, J., Xing, H., and Chiang, C., 2020. Noise strikes, but signal wins in full waveform inver-
619 sion, *SEG Technical Program Expanded Abstracts*, 805–809.

- 620 Issa, N.A., Lumley, D., and Pevzner, R., 2017. Passive seismic imaging at reservoir depths using ambient
621 seismic noise recorded at the Otway CO2 geological storage research facility: *Geophys. J Int.*, **209**(3),
622 1622–1628.
- 623 Jiang, C., and Denolle, M.A., 2020. NoisePy: A new high-performance python tool for ambient-noise
624 seismology: *Seis. Res. Lett.*, **91**(3), 1853–1866.
- 625 Klein, G., 2003. Acquisition and inversion of dispersive seismic waves in shallow marine environments:
626 PhD Dissertation, Universität Kiel.
- 627 Krone, R., 1997. Sismique onde en faible profondeur d'eau: Propriétés de cisaillement des sédiments
628 marins superficiels par inversion simultanée de la dispersion des ondes de Love et de Scholte: Ph.D. dis-
629 sertation, Université de Bretagne Occidentale.
- 630 Kugler, S., Bohlen, T., Forbriger, T., Bussat, S., and Klein, G., 2007. Scholte-wave tomography for
631 shallow-water marine sediments, *Geophys. J Int.*, 551–570.
- 632 Lecocq, T., Caudron, C., and Brenguier, F., 2014. MSNoise, a Python package for monitoring seismic
633 velocity changes using ambient seismic noise: *Seismol. Res. Lett.*, **85**(3), 715–726.
- 634 Linville, A.F., 1994. Single-channel digital filter design for seismic applications: *Geophysics*, **59**(10):
635 1584–1592
- 636 Longuet-Higgins, M.S., 1950, A theory of the origin of microseisms: *Philosophical Transactions of the*
637 *Royal Society of London*, Series A, 243, 1–35.
- 638 Luu, K., 2021. disba: Numba-accelerated computation of surface wave dispersion.
639 <https://github.com/keurfonluu/disba>. Version 0.5.2. Online; accessed 17 October 2021; DOI:
640 10.5281/zenodo.3987395
- 641 McEvelly, T.V. and Majer, E.L., 1982. ASP: An Automated Seismic Processor for microearthquake net-
642 works: *Bulletin of the Seismological Society of America*, **72**(1), 303.
- 643 Nakata, N., Snieder, S., Tsuji, T., Larner K., and Matsuoka, T., 2011. Shear wave imaging from traffic
644 noise using seismic interferometry by cross-coherence, *Geophysics*, **76**(6), SA97–SA106.
- 645 Nakata, N., Chang, J. P., Lawrence, J. F. and Boué, P., 2015, Body wave extraction and tomography at Long
646 Beach, California, with ambient-noise interferometry: *J. Geophys. Res. Solid Earth*, **120**, 1159–1173.
- 647 Nguyen, L. C., Levander, A., Niu, F., Morgan, J., and Li, G., 2022, Insights on formation of the
648 Gulf of Mexico by Rayleigh surface wave imaging: *Geochemistry, Geophysics, Geosystems*, **23**(12),
649 e2022GC010566.
- 650 Olofsson, B., 2010. Marine ambient seismic noise in the frequency range 1-10 Hz: *The Leading Edge*, **29**,
651 418–435.
- 652 Pérez Solano, C. and R.-É. Plessix, 2023, Can elastic waveform inversion benefit from inverting multi-
653 component data?, *The Leading Edge*, **42**(3), 184–189.
- 654 Prieto, G.A., Lawrence, J.F., and Beroza, G.C., 2009. Anelastic Earth structure from the coherency of the

- 655 ambient seismic field, *Journal of Geophysical Research: Solid Earth*, **114**(B7).
- 656 Prieto, G.A., Denolle, M., Lawrence, J.F., and Beroza, G.C., 2011. On amplitude information carried by
657 the ambient seismic field: *C. R. Geoscience*, **343**, 600–614.
- 658 Rauch, D., 1986. On the role of bottom interface waves in ocean seismo-acoustics: A review: in Akal, T.,
659 and Berkson, J. M., Eds. Ocean seismo-acoustics low frequency underwater acoustics: *NATO Conference*
660 *Series 4*, 623–642.
- 661 Ritzwoller, M.H., and Levshin, A.L., 2002. Estimating shallow shear velocities with marine multicompo-
662 nent seismic data: *Geophysics*, **67**(06), 1991–2004.
- 663 Roende, H., Bate, D., Mao, J., Huang, Y., and Chaikin, D., 2020. New node acquisition design delivers
664 unprecedented results with Dynamic Matching FWI — case study from the Gulf of Mexico: *First Break*,
665 **38**(9), 73–78.
- 666 Sager, K., Ermert, L., Boehm, C., Fichtner, A., 2018. Towards full waveform ambient noise inversion,
667 *Geophys. J Int.*, **212**(1), 566–590.
- 668 Schirmer, F., 1980. Experimental determination of properties of the Scholte wave in the bottom of the
669 North Sea, in Kuperman, W. A., and Jensen, B., Eds. Bottom-interacting ocean acoustics: *NATO Confer-*
670 *ence Series 4*, 285–298.
- 671 Shen, Y., Ren, Y., Gao, H., and Savage, B., 2012, An Improved Method to Extract Very-Broadband Empir-
672 ical Green’s Functions from Ambient Seismic Noise, *Bulletin of the Seismological Society of America*,
673 **102**(4), 1872–1877.
- 674 Shi, C., Ren, H., and Chen, X., 2023, Dispersion inversion for P- and S-wave velocities based on guided P
675 and Scholte waves, *Geophysics*, **88**(6), R721-R726.
- 676 Stephen, R.A., 1998. Ocean seismic network seafloor observatories: *Oceanus*, **41**(1), 33
- 677 Stoll, R., and Bautista, E., 1994. New tools for studying seafloor geotechnical and geoacoustic properties:
678 *J. Acous. Soc. Am.*, **96**, 2937–2944.
- 679 Stoll, R., Bryan, G., and Mithal, R., 1991. Field experiments to study seafloor seismo-acoustic response:
680 *J. Acous. Soc. Am.*, **89**, 2232–2240.
- 681 Wapenaar, K., 2004. Retrieving the elastodynamic Green’s function of an arbitrary inhomogeneous
682 medium by cross correlation: *Phys. Rev. Lett.*, **93**, 254301-254305.
- 683 Wapenaar, K., van der Neut, J., Ruigrok, E., Draganov, D., Hunziker, J., Slob, E., Thorbecke, J., and
684 Snieder, R., 2011. Seismic interferometry by crosscorrelation and by multidimensional deconvolution: a
685 systematic comparison: *Geophys. J Int.*, **185**(3), 1335-1364.
- 686 Webb, S.C., 1998. Broadband seismology and noise under the ocean: *Reservoir Geophysics*, **36**, 105–142.